

Physical and Optical Properties of Persistent Contrails: Climatology and Interpretation

Hironobu Iwabuchi¹, Ping Yang^{1*}, K. N. Liou², Patrick Minnis³

¹Department of Atmospheric Sciences, Texas A&M University, College Station, TX

²Joint Institute for Regional Earth System Science and Engineering, and Department of Atmospheric and Oceanic Sciences, University of California, Los Angeles, CA

³Atmospheric Sciences, NASA Langley Research Center, Hampton, VA

For publication in the
Journal of Geophysical Research – Atmosphere

Corresponding author address: Prof. Ping Yang, Department of Atmospheric Sciences,
Texas A&M University, College Station, TX 77843-3150, E-mail: pyang@tamu.edu;
Tel: 979-845-4923

Abstract

Accurate estimations of contrails and contrail cirrus radiative forcing have been limited by substantial uncertainties in the cloud physical and optical properties. A study of the microphysical and optical properties of persistent contrails has been conducted based on measurements made by the Moderate Resolution Imaging Spectroradiometer (MODIS) and the Cloud-Aerosol Lidar and Infrared Pathfinder Satellite Observations (CALIPSO) lidar. MODIS data were used to determine contrail locations and identified contrails analyzed with collocated CALIPSO lidar data. The statistics of the geography, geometry, meteorology, and optical properties are reported for approximately 3400 persistent contrails observed over North America, the North Atlantic Ocean, Greenland, and Europe. The majority of contrails appear in ice-supersaturated air with temperatures lower than -40°C . On average, contrails have significantly larger backscattering coefficients and slightly higher depolarization ratios than neighboring cirrus clouds. Depolarization tends to be high when ice crystals are small and the depolarization ratio is approximately 0.4–0.45 in young contrails and contrail cores. The mean depolarization ratio for contrails increases with decreasing temperature and does not strongly depend on the lidar pointing angle. The backscattering properties suggest that contrails are composed of small, randomly oriented ice crystals containing a few (but non-negligible) horizontally oriented plates. Most contrails are optically thin with optical depths ranging from 0.05 – 0.1; however, optically thicker contrails do exist and tend to grow in warmer and more humid ambient air. The mean value and variation range of the observed depolarization ratio data are consistent with theoretical predictions based on a mixture of nonspherical ice crystals randomly oriented in the atmosphere.

1. Introduction

Contrails formed from aircraft exhaust comprise an important component of aviation's impact on the terrestrial climate system because of perturbations in the radiation budget and hydrological cycle of the Earth-atmosphere system. The annual-mean global coverage of line-shaped contrails is small (about 0.1% for the year 2002); however, regional coverage can be much higher (about 2% in the United States and Europe) over active air traffic areas [*Burkhardt and Karcher, 2009; Palikonda et al., 2005; Rap et al., 2010*]. Contrails may cool the surface during daytime but have a net warming effect on the atmosphere-surface system, i.e., positive radiative forcing at the top of atmosphere [*Meerkotter et al., 1999*]. Persistent, line-shaped contrail global radiative forcing is estimated to be 0.012 W m^{-2} for the years 1992–2005 with uncertainties in the range of $0.005\text{--}0.026 \text{ W m}^{-2}$, but with little understanding of the science involved [*Karcher et al., 2010; Lee et al., 2009; Minnis et al., 2004*]. In the next decades, the regional and global climatic impact of aviation-related emissions is likely to continue increasing at a rapid rate [*Marquart et al., 2003*]. The largest uncertainties in assessing contrail radiative forcing have been caused by a lack of knowledge of both contrail coverage and the optical thickness of persistent contrails [*Karcher et al., 2010; Rap et al., 2010; Schumann, 2002*].

Schumann [2002] and *Heymsfield et al. [2010]* reviewed contrail microphysical properties and evolution. Contrail evolution can be divided into three phases: jet (about 20 sec), vortex (about 2 min) and dispersion (up to hours) phases. Contrails are generated when warm exhaust gases mix with cold ambient air resulting in liquid saturation with the droplets freezing instantly (within 0.1 sec). During the vortex phase, contrail ice crystals are trapped in aircraft wing edge generated vortexes and a significant fraction sublimate from adiabatic heating caused by the descending motion of the vortex system. The fraction of crystals surviving the vortex phase depends primarily on the relative humidity, temperature, and aircraft type [*Sussmann and Gierens, 1999; 2001*]. Based on in situ sampling of ice particles in fresh contrails (age < 2 min), these particles are usually small with a high number concentration [*Baumgardner and Gandrud, 1998; Febvre et al., 2009; Gayet et al., 1998; Goodman et al., 1998; Petzold et al., 1997;*

Schroder et al., 2000]. In many cases, the ice crystal shape in fresh contrails has been reported as quasi-spherical [*Febvre et al.*, 2009; *Gayet et al.*, 1998; *Schroder et al.*, 2000]. In some cases, measurements by a polar nephelometer at the initial stage (age ~1–3 min) indicate that the spherically shaped ice particle model can explain the scattering phase function [*Febvre et al.*, 2009; *Gayet et al.*, 1998]. However, in fresh contrails (age ~1 min), very small (diameter ~1 μm) nonspherical ice crystals with approximately identical shapes have been reported in measurements during the Subsonic Aircraft Contrail and Cloud Effects Special Study (SUCCESS) campaign [*Goodman et al.*, 1998; *Liou et al.*, 1998].

A contrail can persist beyond the vortex phase if the ambient relative humidity with respect to ice exceeds 100% (dispersion phase). Aging allows the ice crystal sizes to increase and number concentrations to decrease [*Poellot et al.*, 1999; *Schroder et al.*, 2000]. A high ice crystal number concentration was found to reside at the contrail core and larger ice crystals (diameter >300 μm) to form at the edges from water vapor supplied by humid ambient air [*Heymsfield et al.*, 1998; *Knollenb.*, 1972]. In-situ and remote sensing measurements [*Duda et al.*, 1998; *Heymsfield et al.*, 1998; *Lawson et al.*, 1998] consistently confirm that large ice crystals are present at contrail edges, and the particle size affects the fall speed resulting in height variations. Large ice crystal fallstreaks observed as virga (diffuse structures) occur in aged contrails, and in-situ and remote sensing measurements are consistent with large eddy model simulations [*Atlas et al.*, 2006; *Heymsfield et al.*, 1998; *Jensen et al.*, 1998]. Old contrails are similar in particle size to surrounding cirrus [*Duda et al.*, 1998; *Gayet et al.*, 1996; *Minnis et al.*, 1998; *Schroder et al.*, 2000]. As aging and increased particle size occurs, ice crystals with complicated shapes become dominant and are consistent with the measured phase function deviations from the spherical particle model used in theoretical calculations [*Febvre et al.*, 2009; *Gayet et al.*, 1998; *Lawson et al.*, 1998]. In situ measurements by particle imaging probes found large ice crystal shapes in contrail peripheries to be either regular, such as bullet rosettes and columns, or irregular [*Febvre et al.*, 2009; *Gayet et al.*, 1996; *Gayet et al.*, 1998; *Heymsfield et al.*, 1998; *Lawson et al.*, 1998]. The spatial variations of the microphysical properties within a contrail often make it difficult to derive robust data from in-situ measurements. Persistent contrails may exist for hours and

grow into irregularly shaped cirrus-like clouds defined as “contrail cirrus” [Heymsfield *et al.*, 2010; Minnis *et al.*, 1998]. Non-linear shaped contrails have been difficult to detect from satellite imagery [Minnis *et al.*, 2005]; however, their impact is likely substantial. During the entire lifecycle of contrails and contrail cirrus, aviation-related particles can influence the hydrological process of natural cirrus clouds by competing for water vapor and by providing additional ice nuclei.

Lidar is a powerful tool for the detection and characterization of the spatial structure and microphysical properties of cirrus clouds. In addition to providing data for the study of the evolution and morphology of contrails [Atlas *et al.*, 2006; Freudenthaler *et al.*, 1995; Spinhirne *et al.*, 1998; Sussmann and Gierens, 2001], the depolarization observations have provided useful information on ice crystal size, shape, and orientation [Sassen, 1991]. Freudenthaler *et al.* [1996] used a scanning polarization lidar and found the depolarization ratio (δ), defined as the ratio of the perpendicular to parallel backscattering coefficients, in the contrail vortex phase (age < 1.6 min) increases from 0.1 to 0.5 and is associated with an increase in temperature from -60 to -50°C . Contrails in the dispersion phase had a depolarization ratio of approximately 0.5. Sassen and Hsueh [1998] reported the depolarization ratio in contrails ranged from 0.3 to 0.7. Compared to natural cirrus clouds, which normally have δ values in the 0.3–0.5 range, some contrails had unusually large depolarization ratios ($\delta > 0.5$). The δ values based on the work of Del Guasta and Niranjana [2001], who analyzed 61 contrails, range from 0.33 to 0.82. Langford *et al.* [2005] found δ tended to be large at the top of contrails, whereas the profile-mean δ was quite small with values of 0.15–0.25. These measurements were limited to either field campaigns or specific areas and temporal periods. The statistics of the contrail depolarization properties are yet to be developed.

In the shortwave region, the radiative forcing of contrails and contrail cirrus is significantly affected by ice crystal size and shape [Meerkotter *et al.*, 1999; Rap *et al.*, 2010]. For this reason, our limited knowledge of ice crystal characteristics in these clouds must be improved in order to more reliably quantify the radiative impact of aviation-induced cloudiness [Yang *et al.*, 2010]. In this study, we have used data from the Cloud-Aerosol Lidar with Orthogonal Polarization (CALIOP) on board the Cloud-Aerosol Lidar and Infrared Pathfinder Satellite Observations (CALIPSO) satellite in conjunction with

observations by the Moderate Resolution Imaging Spectroradiometer (MODIS) to investigate contrail properties in order to provide statistically significant results and substantial geographical coverage.

This paper is organized into 5 sections. A methodology of MODIS-CALIOP collocated data analysis is presented in Section 2. The analysis results from two years of data are presented in Section 3. Observational results of the backscattering properties are compared with theoretical predictions and the microphysical properties of contrail ice crystals are discussed in Section 4. Section 5 presents conclusions based on this study.

2. Methodology

2.1. Data

The Aqua and CALIPSO satellites provide collocated observations with a small temporal difference (~ 75 sec). Since contrails are usually thin and narrow, level 1B data with full spatial resolution are necessary for this study. Contrail locations were determined from the analysis of an Aqua-MODIS image, while the collocated CALIOP level 1B lidar profile data were employed to identify the contrails. We used daytime (afternoon orbits) CALIOP data obtained from quasi-nadir (0.3° off) lidar pointing from the year 2007 and off-nadir (3° off) pointing from 2009. A comparison study based on the two-year data sets was conducted to determine the potential effects of particle orientation on lidar-derived properties.

The selected target region for this study is between latitudes from 20°N to 80°N and longitudes from 180°W to 60°E , including North America, the North Atlantic Ocean, Greenland, and Europe; the areas where contrails most frequently occurred [e.g., *Rap et al.*, 2010]. We acquired MODIS and the corresponding CALIOP data for cases with a high possibility of contrails appearing over MODIS-CALIOP collocated pixels. To find such cases, we individually checked MODIS true color images, composed of three visible wavelength channels with 500-m spatial resolution, available from the MODIS Rapid Response System (<http://rapidfire.sci.gsfc.nasa.gov/>). Collocated MODIS-CALIOP pixels are roughly at the MODIS nadir view. Therefore, we searched for cases with contrails visible near the centerline of the MODIS image. Over the oceans, isolated contrails can

be easily identified. Also, the observation of contrail shadows made it possible to locate contrails over bright polar region ice sheets or homogeneous low-cloud decks. Contrails occur frequently in high-level cloud systems [Sassen, 1997], because the occurrence of contrails is prevalent when the relative humidity is high. Therefore, we also acquired data for cases in which cirrus clouds appeared around the centerline of the MODIS image.

2.2. Detection of contrails in MODIS images

To detect contrails we used the brightness temperature difference (BTD) between the MODIS 11- μm and 12- μm channels. The locations, azimuth directions, lengths, and rough estimates of age were manually determined for each contrail. An automated contrail detection algorithm works well for isolated linear features, but the efficient detection of old-aged, irregular shaped contrails is not easy [Minnis *et al.*, 2005]. For our purpose, manual detection was used to recognize particular patterns, to interpolate disconnected, intermittent contrail segments, and to identify contrails with transformed shapes. Manual processing has led to the positive identification of contrails, although at the expense of the total number of cases to be selected for our studies.

The top panel in Fig. 1 shows an example of a BTD image, with five hand-drawn lines (denoted by A, B, C, D, and E) superimposed on possible contrails that cross a CALIPSO track. Collocated MODIS-CALIOP pixels (denoted by cyan lines) were determined by using the geolocation information recorded in the MODIS and CALIOP datasets. Contrails A and B can be regarded as young because of linear shapes with sharp edges, but contrails C, D and E are more likely to be mature. Contrail C is dim near the MODIS-CALIOP collocated pixel but eastward and westward portions suggest the possibility of its being detectable in a CALIOP profile. Contrail D has a distinct artificial appearance and a width of about 5 km near the MODIS-CALIOP collocated pixel where the large BTD suggests a relatively large optical thickness. Theoretically, the BTD should increase almost linearly with increasing optical thickness up to values of about 1 [e.g., *Betancor-Gothe and Grafl*, 1993]. Other cloud features could be natural cirrus clouds or significantly aged contrails (contrail cirrus) that no longer have a distinct contrail appearance. In practical data processing, we found many dim features that might be contrails, such as indistinct lines embedded in extended cirrus clouds, extrapolated parts

from distinct linear contrails, and faintly thin features between two distinct contrail segments, both of which could possibly be associated with the same aircraft. We considered these features as contrails, because lidar is the best tool to identify a multilayered cirrus cloud system as well as optically thin cirrus. Around contrail B, we see a dim, linear shaped feature, spread to a width of more than 10 km and located in the same direction as contrail B, which appears to be an aged contrail. However, we discarded this type of feature because of low confidence. For each contrail, we estimated a length from the beginning to the end points of a contrail feature that appeared continuous in the MODIS image. The computed length can be considered as a minimum estimate, because in addition to frequent contrail intermittency, the exact beginning and end points might have occurred outside the limits of the MODIS image.

We classified contrails into three types; young, mature, and old based on the morphology in terms of contrail width, shape (linear or transformed shape), and edge sharpness. A young contrail was identified by four criteria: a linear shape, sharp edges, a width approximately less than 3 km, and a maximum distance less than 200 km from the head. Assuming a flight speed of 900 km hr^{-1} , the distance from the head corresponds to an approximate age less than 13 min. The width of this contrail type was frequently smaller than the MODIS pixel size (1 km) such that the contrail appeared as a dotted or dashed line in the BTM image. The type separation of mature and old contrails is more uncertain. A relatively distinct feature with slightly diffusive edges, a linear shape, and an approximate width less than 7 km was classified as a mature contrail. We observed a tendency for mature contrails to have larger BTM values than old contrails. The remaining contrail features were all classified as old contrails. For old contrails, a line-like shape was not obvious on a small spatial scale (roughly 50 km); however, on a large scale ($>100 \text{ km}$), the linear (or curved) shape was apparent and could be easily distinguished from natural cirrus.

Age estimation of mature and old contrail types is difficult, partly because the width depends not only on age, but also on ice-supersaturated layer thickness and wind shear perpendicular to the contrail direction [*Jensen et al.*, 1998]. If a thick contrail has been evolved in a deep ice-supersaturated layer, it can spread horizontally by both wind shear and aging. Using scanning lidar measurements, *Freudenthaler et al.* [1995] derived

a horizontal spreading rate ranging from 18 to 140 m min⁻¹ in the initial 1 hr of the contrail life cycle. Observational results with support by model simulations suggest that the contrail width at 1 hr of age may vary from 1 to 10 km [Jensen *et al.*, 1998; Unterstrasser and Gierens, 2010]. Taking these factors into consideration, the ages of our manually classified mature contrails is likely to be between 13 min and 1–2 hrs.

Excluding the very new (age < 2 min) and short-lived contrails that disappear in dry air, essentially all of the contrails we analyzed could be considered persistent contrails. From the perspective of climatic effects, persistent contrails are more important than short-lived contrails, because of larger areal coverage and longer lifetime. For example, the global coverage of short-lived contrails has been estimated to be extremely small [Ponater *et al.*, 1996].

2.3. CALIOP data processing and identification of contrails

The horizontal and vertical resolutions of CALIOP level 1B data are 1 km and 60 m, respectively, at altitudes between 8 and 20 km. The original data have a higher spatial resolution in the lower atmosphere. We averaged lidar backscattering results to obtain uniform horizontal and vertical resolutions of 1 km and 60 m for the atmosphere below 20 km. CALIOP data included the total and perpendicular attenuated lidar backscattering coefficients at a wavelength of 532 nm (β'_{532} and β'_{532s} , respectively) and the total attenuated backscattering coefficient at 1064 nm (β'_{1064}).

In preprocessing, we identified clouds as cross sectional segments where the attenuated backscattering coefficient is large such that $\beta'_{532} + \beta'_{1064} > 0.003 \text{ km}^{-1}\text{sr}^{-1}$. Any isolated feature with a width less than 1 km and a thickness less than 60 m was regarded as noise. To obtain signals with regards to particulates (e.g., ice crystals), the scattering contribution by molecules and attenuation by ozone were corrected by using the methods developed in previous studies [Vaughan *et al.*, 2010; Hostetler *et al.*, 2005]. When solving the lidar equation, we initially assumed a lidar extinction-to-backscattering ratio (S) of 25 sr, which was a reasonable average value for contrails and optically thin natural cirrus [Langford *et al.*, 2005; Sassen and Comstock, 2001]. According to previous studies, the lidar ratio depends on both cloud type and temperature. We will revisit this

issue in Section 4. Referring to several studies [*Hostetler et al., 2005; You et al., 2006*], we assumed the multiple scattering parameter to be $\eta = 0.7$. The multiple scattering parameter is included in an effective lidar ratio $S' = \eta S$. With the initial assumption of $S = 25$ sr, the lidar equation is solved by a simple iterative algorithm, from the top to the bottom of a cloudy layer. If either a solution diverges or a negative value of the backscattering coefficient is obtained, the lidar ratio is adjusted slightly and the entire cloud layer is recalculated. Total backscattering coefficients at two wavelengths (β_{532} , β_{1064}), parallel and perpendicular backscattering coefficients at a wavelength of 532 nm (β_{532p} , β_{532s}), and extinction coefficients at 532 nm (κ_{532}) were calculated for each cross sectional element. Optically thin contrail segments with $\kappa_{532} < 0.04 \text{ km}^{-1}$ were regarded as non-cloudy and removed from subsequent analysis. Thus, the optical thickness of a cloud layer can be 0.005 at a minimum, while the optical thickness at cloud edge may be as small as 0.0024. The algorithm tends to be unstable at the lower part of thick cloud layers, so we confined our analysis to the upper part with optical thicknesses less than 1.25 from the top of the uppermost cloud layer. Most contrails appear above other clouds, and their optical thicknesses are usually small. Therefore, minimal attenuation correction effects are expected, particularly for the depolarization ratio. The simple algorithm described was chosen because our main interest is in the depolarization ratio rather than the backscattering coefficient.

With the help of the location information determined from the MODIS data analysis, contrails were searched in the CALIOP profile. The lower two panels in Fig. 1 show CALIOP profiles in a sample case corresponding to the MODIS image shown in the top panel. Signals from non-cloudy elements are masked in the plots shown in Fig. 1. Contrails were identified based on the limited vertical extent with substantial backscattering, as compared with surrounding cirrus. Red vertical lines in the plots denote contrail locations detected by the MODIS image analysis. Young contrails A and B were isolated from cirrus clouds, with confined widths within 1–2 km. The vertical extent is approximately 250 m for A and 450 m for B. A cirrus cloud with a width of about 30 km was present just beneath contrail B and found as a dim feature in the MODIS image. Contrail C is not clearly exhibited in this profile, and we rejected the

sample. Contrail D is embedded in cirrus, contrail E extends from cirrus, and both are mature with moderate vertical and horizontal extents.

Contrails do not always occur perpendicular to the CALIPSO track. The apparent contrail width (W) in a lidar profile is corrected by considering an angle (ϕ) between the contrail and CALIPSO track directions. A corrected width is given by

$$W = W' \sin \phi. \quad (1)$$

Contrail identification was done semi-automatically with contrail core centers identified by maxima in β_{532} within 7 km from the location diagnosed in the MODIS analysis. The 7 km tolerance is from location error due to the hand drawing, uncertainties in the location matching between MODIS and CALIOP data, and location differences between peaks of the BTD and the β_{532} . Subsequently, a cluster of cloudy elements surrounding the core center was identified. Determining contrail boundaries embedded in or extending from cirrus is uncertain and possibly erroneous. The contrail width was restricted not to exceed 3 km, 7 km, and 21 km, respectively, for young, mature, and old contrails. We assumed that β_{532} within a contrail should decrease with increasing distance from the core center. The surrounding cirrus volumes are discriminated as cross sectional elements with $\beta_{532}(\Delta x, \Delta z)$ larger than a threshold β_{\min} , where Δx and Δz are horizontal and vertical distances from the core center. The threshold is given by the two-dimensional Gaussian distribution

$$\beta_{\min} = \frac{\beta_{peak}}{\pi \sigma_x \sigma_z} \exp \left\{ -\frac{1}{2} \left[\left(\frac{\Delta x}{\sigma_x} \right)^2 + \left(\frac{\Delta z}{\sigma_z} \right)^2 \right] \right\}, \quad (2)$$

where β_{peak} is the β_{532} value at the core center, and standard deviations σ_x and σ_z are manually determined for each contrail. In practice, the determination of contrail boundaries was difficult when a contrail with no distinct clustering of large β_{532} was embedded in an optically thick cirrus layer. Cases where the identification of a contrail was difficult were excluded from subsequent analysis; 21% of the contrails detected in the MODIS data analysis were rejected in the CALIOP data analysis.

2.4. Averaging and statistics calculations

Properties of cirrus clouds adjacent to contrails are of particular interest because they appear under unique meteorological conditions. We defined neighboring cirrus as those present within a horizontal distance of 150 km and a vertical distance of 1.5 km from the contrail core center. The neighboring cirrus clouds in our analysis were not necessarily natural. Some could be old-aged contrails that no longer had a contrail-like shape, while others could be cirrus indirectly influenced by either contrail particles or gases and aerosol particles from aircraft exhausts.

The backscattering coefficients were integrated for cross sectional elements of a contrail and the neighboring cirrus clouds, and used to compute average values. The contrail/cirrus-integrated depolarization ratio (δ) and color ratio (χ) were computed by

$$\delta = \langle \beta_{532s} \rangle / \langle \beta_{532p} \rangle, \quad (3)$$

$$\chi = \langle \beta_{1064} \rangle / \langle \beta_{532} \rangle, \quad (4)$$

where an angle bracket denotes integration over cross sectional elements. The near infrared channel (1064 nm) of CALIOP is calibrated with the assumption that strongly scattering cirrus clouds have a color ratio of 1.0 as described in Hostetler et al. [2005]. Vaughan et al. [2010] confirmed that the typical color ratio for a dense natural cirrus cloud is very close to 1.0. We investigated a possible color ratio difference between contrails and neighboring cirrus clouds and computed the optical thickness (τ_{532}) at a wavelength of 532 nm for each contrail column. Other analyzed quantities include latitude, altitude, width, height, temperature, and relative humidity with respect to ice (RH_{ice}). We used meteorological data (pressure, temperature, relative humidity, and molecular and ozone number densities) included in the CALIPSO data set, which was originally obtained from the Global Modeling and Assimilation Office [*Hostetler et al.*, 2005].

3. Observational results

3.1. Geography, geometry and meteorology

Figure 2 shows geographical locations of identified contrails. Many contrails are located over the North Atlantic, especially over the major flight corridors between the United States and Europe. High concentrations are noted in Western Europe, the southern part of Greenland, and the eastern part of North America. It should be noted that our data sampling is neither seasonally nor spatially homogeneous. Aqua and CALIPSO satellites cover high latitude regions, but winter data were not available over polar regions on the MODIS Rapid Response System website. The contrails in our analysis are concentrated over the oceans, but coverage of the line-shaped contrails estimated from climate model simulations is higher over land in the United States and Europe than those over oceanic regions [Burkhardt and Karcher, 2009; Rap et al., 2010].

Table 1 and Fig. 3 summarize the statistics obtained with regards to geometry and meteorological conditions. Contrails mostly appear in the uppermost part of the troposphere with an average mid-level altitude of 10.7 km. Figure 3a shows that the average altitude decreases with increasing latitude. The altitude z (km) and latitude θ ($^{\circ}$) can be represented by a least square fit as follows:

$$z \approx 12.5 - 0.035 \times \theta. \quad (5)$$

In general, contrails appear in cold and supersaturated environments. The average mid-level temperature was -54°C , almost identical to the temperature (-55°C) at extra-tropical cruising altitudes near 200 hPa [Karcher et al., 2009]. The majority of contrails were found in a temperature range between -42 and -63°C , which indicates that contrail formation is primarily related to ice crystal homogeneous nucleation. A small portion of samples were found at temperatures $> -40^{\circ}\text{C}$, which agrees with temperatures reported between -40 to -65°C in most of the 178 contrails observed by Sassen [1997] over Salt Lake City, Utah, USA. The mid-level RH_{ice} values for this dataset yield an average of 126% and are distributed as shown in the histogram of Fig. 3b. Of all contrails, 13% occurred in sub-saturated conditions ($\text{RH}_{\text{ice}} < 100\%$) according to the GMAO analyses and are believed to be either short-lived or to have occurred in supersaturated conditions. The majority of contrails detected in our MODIS and CALIOP data analysis are considered

persistent and require an ambient RH_{ice} of at least 100%. Highly supersaturated air ($RH_{ice} > 150\%$), a favorable condition for the formation of natural cirrus, accounted for about 22% of the contrails analyzed. However, the largest contrail population (65%) was found in moderately supersaturated air ($100\% < RH_{ice} < 150\%$).

The contrail average horizontal width obtained from this analysis is 6.5 km with an average thickness of 0.67 km. Figure 3c shows a scatter plot of thickness and width and illustrates frequency discontinuities around the 3- and 7 km widths. We have limited contrail widths by using different maximum values for young and mature contrails, and the discrepancies suggest a need for improvement in contrail boundary identification. Nevertheless, there is a clear positive correlation between thickness (H in km) and width (W in km). The superimposed curve in Fig. 3c is a least-squares fit given by

$$H \approx 1.29 \times W^{0.513}. \quad (6)$$

The width is approximately proportional to the square of the thickness and denotes a mechanism of vertical and horizontal spreading by aging. At the end of the vortex phase (about 2 min), contrails can grow vertically to 150–300 m in depth with little horizontal spreading [Schumann, 2002]. Our results show that most contrails appear to have a thickness greater than 180 m. In the dispersion phase, updraft air motion in the contrail core lifts small ice crystals and causes the large ice crystals formed at the edges to fall quickly, resulting in the vertical spreading of contrails [Jensen *et al.*, 1998]. Ice crystals falling below the bottom of a supersaturated layer evaporate, thus, the depth of the ice-supersaturated layer limits the vertical depth [Freudenthaler *et al.*, 1995]. Figure 4 shows the average contrail thickness as a function of mid-level RH_{ice} and width. There is a tendency for thickness to increase with increasing mid-level RH_{ice} , because thick contrails can develop in highly supersaturated air owing to the faster growth and sedimentation of large ice particles. The horizontal spreading of persistent contrails is typically determined by wind shear [Jensen *et al.*, 1998; Karcher *et al.*, 2009; Unterstrasser and Gierens, 2010]. If supersaturation is present in a thick layer, wind shear can effectively make the contrail spread in the horizontal direction. Thus, the contrail width depends on the ice-supersaturated layer depth, wind shear, and age. Table 3 presents the geometrical size statistics for the three contrail types: young, mature, and old.

Estimates of width and thickness strongly depend on the threshold for contrail boundary determination. Model simulation results of *Karcher et al.* [2009] indicate the average width of a contrail aged between 2 min and 4 hours can be large (18–19 km) if very optically thin parts of the contrail are included. The average width (6.5 km) in our results is only one third of *Karcher et al.*'s value, which indicates the inherent difficulty in defining contrail boundaries. On the other hand, the limited horizontal resolution of CALIOP can positively bias the width, because the contrail volume may only partly cover a cross sectional element of a CALIOP observation. The partial coverage may introduce a positive bias of 0–2 km to the width estimate with an average bias of about 1 km. If we assume the bias is due to partial coverage, the corrected average widths of young, mature, and old contrails should have been 1.5, 4.1, and 11.3 km, respectively. The relative impact on the estimated width could be substantial in young contrail cases and result in uncertainties in both the width and thickness estimates. Nevertheless, high-resolution lidar measurements in Southern Germany [*Freudenthaler et al.*, 1995] revealed widths of persistent contrails (age < 60 min) at 1.5–3 km, which are consistent with our results.

The average contrail length is 264 km with a large standard deviation. Figure 3d shows a length histogram with a strongly skewed distribution and a peak at 50–100 km. Contrail length statistics are considered to represent the horizontal extent of a continuously ice-supersaturated region at cruise altitude. Approximately 1.5% of our samples were longer than 1000 km.

3.2. General statistics of lidar-derived optical properties

Table 2 summarizes the statistics of lidar-derived optical properties for contrails and the neighboring cirrus clouds, Table 3 summarizes type-specific contrail properties, and Fig. 5 visually displays average values. As shown, contrails exhibit much larger backscattering coefficients (by about twofold) and slightly higher depolarization ratios than neighboring cirrus clouds. The average depolarization ratios were 0.393 and 0.439 in quasi-nadir and off-nadir observations. The typical values of contrail depolarization ratios lie in the range of 0.3–0.55, which is generally consistent with some previous ground based lidar measurements for dispersion phase contrails [*Del Guasta and Niranjan*, 2001;

Freudenthaler et al., 1996; *Sassen and Hsueh*, 1998; *Sussmann and Gierens*, 2001]. The same depolarization range is also typical for natural cirrus ice crystals [*Sassen*, 1991; *Sassen and Benson*, 2001; *Sassen and Zhu*, 2009]; however, the non-negligible differences in depolarization between contrails and neighboring cirrus clouds indicate some variations are present in the microphysical properties. Young contrails were found to have large backscattering coefficients and high depolarization ratios. The large contrail backscattering coefficient implies a high ice crystal number concentration, which is confirmed by in situ measurements in contrails aged 10–30 min [*Sassen*, 1997; *Schroder et al.*, 2000]. Assuming the backscattering phase function value to be about the same, a significantly high number concentration should make up for the large backscattering coefficients and compensate for the cross section of small particles dominant in young contrails. Old contrails had smaller backscattering coefficients and lower depolarization ratios with values close to those of the neighboring cirrus clouds. Thus, aged contrails and neighboring cirrus clouds may have similar microphysical properties. The size distribution of old contrails (> 60 min) develops into the general cirrus distribution [*Schroder et al.*, 2000].

Contrail cores are known to have a high number concentration of small particles, and large falling particles with a small number concentration make up fall streaks [*Atlas et al.*, 2006; *Heymsfield et al.*, 1998; *Lawson et al.*, 1998; *Unterstrasser and Gierens*, 2010]. For each contrail, we classified the cross sectional elements into core or periphery areas. A core was defined as having a larger β_{532} than the median value, and the remaining elements were identified as peripheries. Often found in old contrails were virga with a small β_{532} beneath a core with a large β_{532} . As shown in Fig. 5, contrail cores have higher average depolarization ratios than peripheries. Thus, it appears that backscattering by small particles in the cores is strongly depolarized.

Specular reflections from the smooth faces of ice particles can produce strong backscattering with no depolarization. Large plates (diameter > 100 μm) tend to fall with their major axes oriented horizontally. Thus, it is generally accepted that strong backscattering with weak depolarization observed by vertically pointing lidars are generated by horizontally oriented plates [*Sassen and Benson*, 2001]. If the lidar is pointing a few degrees off nadir, the effects of specular reflection are significantly

reduced. As shown in Fig. 5, quasi-nadir observations yield a larger average β_{532} and lower average δ than off-nadir observations and are particularly noticeable in cirrus clouds. Differences in the average δ by the pointing angle were about 11% for contrails and as large as 25% for neighboring cirrus clouds. For young, mature, and old contrails, the corresponding differences are 8%, 11% and 15%, respectively. The influence of horizontally oriented plates is evidently stronger in old contrails and cirrus clouds than in young contrails.

The average optical thicknesses are 0.24 and 0.19 in quasi-nadir and off-nadir observations. The optical thickness difference of approximately 30% measured by the pointing angle reveals the average backscattering coefficient variation from assuming a constant lidar ratio independent of the pointing angle. The optical thickness standard deviation was almost the same as the average, indicating a large diversity in this quantity. The partial coverage by a contrail over cross sectional elements in a lidar profile can introduce a positive bias in the width and a negative bias in the optical thickness. The relative impact of partial coverage should be larger for narrower contrails. The optical thickness of a contrail with an actual width of 1.5 km can be 66% larger than an estimate that included partial coverage, assuming a bias of 1 km in the width estimate. Thus, young contrails should have larger optical thicknesses than old contrails, as demonstrated by large eddy model simulations [*Unterstrasser and Gierens, 2010*].

There is no significant difference in the color ratio between contrails and neighboring cirrus. Young contrails tend to have slightly lower color ratios than old contrails. Difference in the color ratio by the pointing angle was unexpected, which could be linked to the calibration algorithm of the 1064-nm channel of CALIOP, several assumptions (especially, the effective lidar ratio) in the attenuation correction procedure, and the presence of horizontally oriented particles.

Figure 6 shows two-dimensional histograms of total backscattering coefficients at 532 nm and the depolarization ratios. Contrails generally show no significant correlation between these two parameters, but a negative correlation is exhibited for cirrus. In quasi-nadir observations (Fig. 6a), a significant fraction (38%) of cirrus clouds have $\delta < 0.3$ associated with strong backscattering, but in contrast, only 18% of contrails have $\delta < 0.3$. In previous quasi-nadir observations studies [*Cho et al., 2008; Hu et al., 2007*], the

negative correlation was typical in cold ice clouds. Our results suggest the presence of horizontally oriented plates in many cirrus cases. In the off-nadir observations (Fig. 6b), the contrail depolarization ratio has a narrow distribution between 0.3 and 0.55, but contrails and the neighboring cirrus rarely have $\delta < 0.3$. The depolarization ratio of contrails does not strongly depend on the pointing angle, therefore, contrails may have fewer horizontally oriented particles than cirrus.

For fresh contrails in the vortex phase (age < 2 min), *Freudenthaler et al.* [1996] suggested a rapid change of the depolarization ratio with age. Low δ values can be associated with very small nonspherical particles (diameter $< 1 \mu\text{m}$) and agree with the theoretical results derived by *Mishchenko and Sassen* [1998]. In our results, the majority of contrails are in the dispersion phase (> 2 min) and exhibit high δ values with rare low δ values and are consistent with the results for persistent (> 2 min) contrails from *Freudenthaler et al.* [1996]. *Del Guasta and Niranjana* [2001] have reported rare cases of aged contrails with $\delta < 0.25$, in agreement with our results. Under low ambient relative humidity, *Sassen* [1979] and *Sussman* [1997] reported halos and perhelions in the aged (> 30 min) contrails and predicted horizontally oriented hexagonal plates with diameters of 300–2000 μm . Although our results support the presence of horizontally oriented plates in contrails, the population fraction is smaller than in neighboring cirrus.

Figure 7 presents a comparison between contrail peripheries and cores. The cores are associated with high δ values between 0.3 and 0.5 from quasi-nadir observations and between 0.35 and 0.55 from off-nadir observations. Compared to the cores, peripheries have widely scattered and lower δ values. The off-nadir results (Fig. 7b) yield broader distributions than those seen in the nadir-view values (Fig. 7a).

Figure 8 shows two-dimensional histograms of total backscattering coefficients and color ratios. The average color ratios of contrails and neighboring cirrus clouds are substantially the same, and in both cases, total backscattering coefficients and color ratios are negatively correlated. *Vaughan et al.* [2010] reported a similar negative correlation for natural cirrus clouds. Large backscattering coefficients tend to appear in young contrails and in contrail cores, where small ice crystals associated with low color ratios are likely to dominate.

3.3. Depolarization ratio: Dependence on altitude, temperature, and thickness

Figure 9 shows the depolarization ratio dependence on altitude, temperature, and geometrical thickness. The depolarization is stronger at higher altitudes. A steady increase in the depolarization ratio with decreasing temperature (Fig. 9b) is similar to that of neighboring cirrus (Fig. 9d). Similar temperature dependencies have been reported in previous observational studies for natural cirrus clouds [Reichardt *et al.*, 2002; Sassen and Comstock, 2001; Sassen and Zhu, 2009]. According to model predictions, ice crystals have large sizes when the ambient temperature is high [Unterstrasser and Gierens, 2010]. Large particles formed at higher temperatures appear to be associated with weaker depolarization.

The depolarization ratio is high in geometrically thin contrails (Fig. 9c), which can be considered as relatively young contrails. A dependence of δ on thickness indicates ice crystal growth and variations in shape and orientation. The depolarization ratio may be larger than 0.6 in geometrically thin (< 0.8 km), relatively young contrails. Sassen and Hsueh [1998] reported a strong depolarization ($\delta > 0.5$) is typical of contrails based on observations obtained during the SUCCESS campaign.

For contrails, linear fits for the relationships shown in Fig. 9 are given by

$$\delta \approx 0.194 + 0.0185 \times z, \quad (7)$$

$$\delta \approx 0.022 - 0.00688 \times T, \quad (8)$$

$$\delta \approx 0.483 - 0.135 \times H \quad (9)$$

for quasi-nadir observations and

$$\delta \approx 0.274 + 0.0155 \times z, \quad (10)$$

$$\delta \approx 0.187 - 0.00476 \times T, \quad (11)$$

$$\delta \approx 0.483 - 0.065 \times H \quad (12)$$

for off-nadir observations, where T is the mid-level temperature (K). For cirrus, the temperature dependence can be represented by a linear fit

$$\delta \approx 0.082 - 0.00445 \times T, \quad (13)$$

$$\delta \approx 0.212 - 0.00377 \times T \quad (14)$$

for quasi-nadir and off-nadir observations.

Figure 10 shows the average depolarization as a function of geometrical thickness and temperature, illustrating that geometrically-thin (probably young), cold contrails have

high δ values. Generally speaking, large depolarization ratios obtained for young contrails, at the contrail core, and at low temperatures are associated with ice crystal size, shape, and orientation. In Section 4, we present the microphysical interpretation of results given here.

3.4. Optical thickness

Figure 11 shows a histogram of contrail optical thickness at the 532-nm wavelength. Horizontally oriented particles have less influence on off-nadir observations and the results are more likely to be statistically representative. In off-nadir observations, about 34% of the contrail columns have $\tau_{532} < 0.1$ with the highest frequency occurrence exhibited at $\tau_{532} = 0.05 - 0.1$. The average contrail optical thickness is 0.19 with a median value of approximately 0.14. A negligible fraction ($< 0.3\%$) have $\tau_{532} > 1$. Thick contrail columns with $\tau_{532} > 0.5$ occupy 5% in off-nadir and 10% in quasi-nadir observations. The large optical thickness range is in line with previous observations [e.g., *Minnis et al.*, 2005]. However, the off-nadir averages are shown to be between those determined from passive satellite retrievals: smaller values over the United States [*Palikonda et al.*, 2005] and larger values over Europe [*Meyer et al.*, 2002].

Comparison with other data sources is not straightforward, partly because the average optical thickness strongly depends on the method applied to contrail identification. *Karcher et al.* [2009] compiled the optical thickness estimates of persistent contrails obtained from satellite observations using passive sensors, ground/aircraft-based lidar measurements, and model simulations. Retrievals using passive satellite imagers typically yield optical thicknesses between 0.01 and 1.0, with 1-2% of the retrievals giving values exceeding 1 [e.g., *Minnis et al.*, 2005]. The lidar measurements show a broader optical thickness range between 0.05 and 2.0. However, compared with previous studies, the current results seem reasonable considering the geographical and seasonal variations. *Atlas and Wang* [2010] reported a contrail having $\tau = 2.3$ observed as an aircraft flew along the wind direction in a region of high humidity relative to ice. Model simulations predict a substantial fraction of 20–50% of subvisible contrails ($\tau < 0.02$) [*Karcher et al.*, 2009; 2010], but our analysis appears to miss a large number of

subvisible contrails. Lidar measurements have the capability to detect subvisible clouds, but separating subvisible contrails from cirrus clouds in CALIOP profiles is extremely difficult and could be the prime reason for the lack of subvisible contrails in this study. Also, it is possible that subvisible contrails may not be as common as the models predict.

Figure 12 shows the optical thickness dependence on the temperature and relative humidity. The sample dispersion is large, but the apparent tendency shows increasing optical thickness with increasing temperature and relative humidity. The ice water content basically depends on the amount of water vapor available for ice crystal formation in ice-supersaturated air. The available water vapor amount is large under warm and humid conditions generating large optical thicknesses consistent with model simulations [Karcher *et al.*, 2009; Palikonda *et al.*, 2005; Unterstrasser and Gierens, 2010]. The temperature (T) and RH_{ice} dependence can be represented by least-square fits as follows:

$$\tau_{532} \approx 0.785 - 0.01 \times T, \quad (15)$$

$$\tau_{532} \approx 0.0995 - 7.01 \times 10^{-4} \times RH_{ice} \quad (16)$$

for quasi-nadir observations and

$$\tau_{532} \approx 0.493 - 0.00575 \times T, \quad (17)$$

$$\tau_{532} \approx 0.157 - 6.43 \times 10^{-4} \times RH_{ice} \quad (18)$$

for off-nadir observations.

4. Interpretation by utilizing theoretical calculations

4.1. Computation descriptions

To interpret the observational results, the single scattering properties of ice particles were simulated based on the Lorenz-Mie theory for ice spheres and the Improved Geometrical Optics Method (IGOM) [Bi *et al.*, 2009; Yang and Liou, 1996] for randomly oriented non-spherical ice crystals. In the scattering calculations, we used nine ice crystal habits: spheres, droxtals, solid/hollow columns, plates, solid/hollow bullet rosettes, aggregates, and irregular shapes. The geometrical representation of each ice crystal habit has been described in Yang *et al.* [2000; 2005]. Particle geometry (e.g., aspect ratio and

hollowness) is size-dependent, and smaller particles generally tend to have more compact geometries with an aspect ratio of approximately 1. Although the theoretical phase function typically exhibits halo features for pristine ice crystals larger than $\sim 40 \mu\text{m}$, the halos have not been commonly observed in the atmosphere [e.g., *Baran, 2009*]. The presence of surface roughness, irregular shapes, and air bubbles in ice particles are possible explanations for featureless phase functions [*Baran, 2009; Nousiainen and McFarquhar, 2004; Shcherbakov et al., 2006; Xie et al., 2009; Yang et al., 2008*]. In this study, the particle surface roughness was assumed from the two-dimensional Gaussian distribution model expressed by a single parameter σ [*Yang et al., 2008*]. In actual cirrus clouds (and contrails), various ice crystal habits and sizes coexist. Thus, the bulk scattering properties should be computed by accounting for both habit fractions and particle size distribution (PSD).

An arbitrary bulk scattering property can be represented by introducing the integral operator,

$$\left\{ \hat{X} \right\}_{bulk} = \int_{D_{min}}^{D_{max}} n(D) \left[\sum_j h_j(D) \hat{X}_j(D) \right] dD, \quad (19)$$

for an arbitrary parameter D representing particle size, a size range between D_{min} and D_{max} , the number density $n(D)$, a size-dependent habit fraction $h_j(D)$ for habit j , and the scattering property $\hat{X}_j(D)$ of a single particle. Using Eq. (19), the scattering efficiency factor Q_{sca} and the phase function P_{11} for an ice crystal habit mixture can be written as

$$Q_{sca} = \left\{ \hat{A}_{sca} \right\}_{bulk} / \left\{ \hat{A}_{geo} \right\}_{bulk}, \quad (20)$$

$$P_{11} = \left\{ \hat{A}_{sca} \hat{P}_{11} \right\}_{bulk} / \left\{ \hat{A}_{sca} \right\}_{bulk}, \quad (21)$$

where \hat{A}_{sca} and \hat{A}_{geo} are scattering and geometrical cross sections of a single ice crystal. The effective diameter D_{eff} is defined by Foot, [1988]; Baum et al., [2005] and references cited therein.

$$D_{eff} = \frac{3}{2} \cdot \left\{ \hat{V} \right\}_{bulk} / \left\{ \hat{A}_{geo} \right\}_{bulk}, \quad (22)$$

where \hat{V} is the volume of a single ice crystal. The lidar and depolarization ratios are given by

$$S = \frac{4\pi}{\omega P_{11}(\pi)}, \quad (23)$$

$$\delta = \frac{P_{11}(\pi) - P_{22}(\pi)}{P_{11}(\pi) + P_{22}(\pi)}, \quad (24)$$

where ω is the single-scattering albedo and the symbol P denotes the scattering matrix elements. These parameters were computed at the visible 532 nm wavelength where $\omega = 1$. The lidar ratio is a function of P_{11} in the backscattering direction. The color ratio is defined by

$$\chi = \frac{Q_{sca,1064} P_{11,1064}(\pi)}{Q_{sca,532} P_{11,532}(\pi)}. \quad (25)$$

The PSD can be represented by the following function:

$$n(D) = N \frac{(D/\nu)^{\alpha-1} \exp(-D/\nu)}{\nu \Gamma(\alpha)} \quad (26)$$

for $D = D_{\min}$ to D_{\max} , where N is particle number concentration, D is the maximum dimension, α is the shape parameter, ν is the scale parameter, and Γ is the Gamma function. We used the values, $D_{\min} = 2 \mu\text{m}$ and $D_{\max} = 10000 \mu\text{m}$. If $\alpha > 0$, $D_{\min} = 0$ and $D_{\max} = \infty$, Eq. (26) obeys the Gamma distribution, where the shape parameter determines the coefficient of variation (standard deviation divided by the mean) and is closely related to the PSD width.

If the ice crystal shape is known, the two parameters, α and ν , can be estimated from any two parameters among the mean/effective particle size, average particle volume, and geometrical/extinction cross section. We used estimates from in situ measurements in contrails and cirrus clouds presented previously [Febvre *et al.*, 2009; Gayet *et al.*, 1996; Goodman *et al.*, 1998; Petzold *et al.*, 1997; Schroder *et al.*, 2000]. The ice crystal shapes were assumed to be exclusively spherical, and although the assumption might introduce errors in the parameter estimation, the present purpose was to investigate a rough relationship between α and ν . In many contrail cases, particularly young contrails, ice crystals were reported to have nearly spherical, quasi-spherical, or compact geometries with an aspect ratio close to 1. Our estimations appear to be reasonable for young contrails.

Figure 13 shows the relationship between α and ν . The cirrus PSD data compiled by *Baum et al.* [2005] were plotted in addition to our contrails and cirrus estimates. Contrails have a large α and a significantly smaller ν compared to those for cirrus clouds. This agrees with a narrow PSD for small particle sizes found for in situ results [*Petzold et al.*, 1997; *Poellot et al.*, 1999; *Schroder et al.*, 2000; *Schumann et al.*, 2010]. The α values generally decrease with increasing ν and broaden the PSD with increasing particle sizes. Large deviations were apparent between samples, and no distinct differences were found between contrails and cirrus clouds. Therefore, a single least-square fit has been developed to include both contrails and cirrus,

$$\alpha + 2 = 6.01 \times \nu^{-0.137}. \quad (27)$$

In determining the coefficients in Eq. (27), we used a tenfold larger weight for our own data than for that of *Baum et al.* [2005]. As shown in Fig. 13, most data lay in the $\alpha + 2$ range either twofold smaller or larger than the fit curve. Eq. (27) is useful because it represents PSDs analytically, and by changing the shape parameter, we can investigate the possible sensitivity between optical properties and PSD width. Preliminary tests showed a twofold change of $\alpha + 2$ resulted in only slight optical property differences when compared with a fixed effective diameter. At a visible wavelength (532 nm), the maximum difference was 1% for the extinction efficiency factor and the asymmetry factor, 2% for the depolarization ratio, and 15% for the lidar ratio.

4.2. Hexagonal ice crystals

Figure 14 shows the lidar, depolarization and color ratios as functions of the effective diameter for hexagonal, polydispersed ice crystals with various aspect ratios ($2a/L$). For smooth ice crystals, the lidar ratio decreases with increasing effective diameter. Compact ice crystals ($2a/L \sim 1$) exhibit the lowest lidar ratio, and in the range of $D_{\text{eff}}=10\text{--}100 \mu\text{m}$, the lidar ratio varies between 5 and 50 sr. The predicted depolarization ratio is sensitive to the aspect ratio but not to the effective diameter. When ice crystals are smooth, both columnar particles ($2a/L < 1$) and plate-like particles ($2a/L > 1$) have high depolarization ratios with values of 0.48–0.55 and 0.28–0.37, respectively. When ice crystals are moderately rough with $\sigma = 0.1$, where σ is a parameter indicating the degree of surface

roughness [Yang and Liou, 1998], compact ice crystals exhibit the strongest depolarization, while aspect ratio deviations from unity result in smaller depolarization ratios. The color ratio is not sensitive to aspect ratio, which have values of 0.5–0.7 for smooth particles and 0.9–1.0 for moderately rough particles. The particle surface roughness has a significant effect on backscattering properties. Supplemental tests showed that with very slight roughness (e.g., $\sigma = 0.001$), the lidar ratio was high (> 50 sr) and not sensitive to the effective diameter, the backscattering peak was smoothed in the phase function, and the color ratio was close to 1.

4.3. Habit mixtures

The dominant contrail ice habits likely depend on particle size. Based on several reports found in the literature, we tested three mixture models with size-dependent habit fractions, as illustrated in Fig. 15. Habit fractions vary linearly with respect to $\log D$ between anchor points at $D = 5, 20, 100, 500,$ and $2000 \mu\text{m}$. In situ measurements showed that the small particles ($D < 50 \mu\text{m}$) found in young contrails and aged contrail cores are either nearly spherical or compact particles [Febvre *et al.*, 2009; Goodman *et al.*, 1998; Schroder *et al.*, 2000]. In our models, the small particles are represented by droxtals [Yang *et al.*, 2005], which are compact faceted particles. In the contrail periphery, large particles, primarily columns with $D < 200 \mu\text{m}$ and bullet rosettes with $D < \sim 300 \mu\text{m}$, were found by Heymsfield *et al.* [1998] and Lawson *et al.* [1998]. The moderate size range of $D = 20\text{--}500 \mu\text{m}$ is the most important for determining optical properties. Thus, we assumed a mixture with columns, plates, and bullet rosettes as the prime components in mixture model 1. In some aged contrail cases, the ice crystal shape has been reported as irregular [Febvre *et al.*, 2009; Gayet *et al.*, 1996; Gayet *et al.*, 1998], and measurements in various ice clouds revealed that irregular ice crystals dominate in the range between 20 to $200 \mu\text{m}$ [Baker and Lawson, 2006; Gallagher *et al.*, 2005; Heymsfield and McFarquhar, 2002; Korolev *et al.*, 2000; Lawson *et al.*, 2006; Whiteway *et al.*, 2004]. The appropriate morphological representation of irregular ice crystals is not well known. In our model, we used an aggregate of hexagonal ice crystals with moderate surface roughness ($\sigma = 0.1$) as a surrogate for an irregular ice crystal. The irregular ice

crystal model does not produce halos and exhibits a smooth phase function with an asymmetry factor of 0.76, which is comparable to quasi-spherical, irregular ice crystals found by *Nousiainen and McFarquhar [2004]*, and a relatively high depolarization ratio of ~ 0.54 . Thus, the habit mixture model 2 included a significant fraction of moderately sized, irregular ice crystals. For comparison purposes, mixture model 3 included many plates instead of columns.

Figure 16 shows computed depolarization ratios for the three habit mixture models as functions of the effective diameter. For all models, the depolarization ratio is in the range between 0.35 and 0.52 and in agreement with the CALIOP observation results obtained from off-nadir pointing data. Model 2 produces slightly larger values of δ than model 1. However, this does not have significant implications because δ may vary depending on the geometrical representation of the irregular particles. Model 3 exhibits a lower value of δ than the others, a result due to the dominance of plates. For smooth ice crystals, the depolarization ratios of models 1 and 2 slightly increase with increasing effective diameter. Except for model 2, rough ice crystals generally produce a decrease in δ with an increase in effective diameter.

Figure 17 shows the relationships between computed depolarization and lidar ratios for each ice crystal habit and habit mixture model, along with a reasonable range determined from observations. The δ ranges are defined as the average plus/minus one standard deviation as obtained from our CALIOP contrail data analysis. We found only one published report of a contrail lidar ratio. *Langford et al. [2005]* observed contrails over Boulder, Colorado and obtained $S = 13\text{--}40$ sr for the majority of the contrails. For optically thin cirrus ($\tau < 1$) in cold air ($T < -40^\circ\text{C}$ approximately), a reasonable range of S is 10 to 50 sr, based on previous studies [*Chen et al., 2002; Immler and Schrems, 2002; Reichardt et al., 2002; Sakai et al., 2003; Sassen and Comstock, 2001*], and which generally agrees with the results of *Langford et al. [2005]*. Figure 17a shows a variety of δ and S pairs depending on the ice crystal habit and the surface roughness. Spherical particles exhibit zero depolarization and $S = 15\text{--}20$ sr. The CALIOP observations suggest ice spheres are not dominant in the persistent contrails analyzed in this study. Except for spheres, only smooth plates have relatively low δ values (0.3–0.36). The other smooth surfaced habits (droxtals, hollow columns, solid/hollow bullet rosettes, and column

aggregates) exhibit higher δ values (0.4–0.57). In most cases, surface roughness does not significantly change the depolarization ratios but results in higher lidar ratios. For most habits, computed lidar ratios of rough particles are beyond the reasonable range. As shown in Fig. 17b, all of the three smooth surfaced habit mixture models exhibit δ and S within reasonable ranges. When surface roughness is present, the lidar ratio is too high for $D_{\text{eff}} > \sim 20 \mu\text{m}$. Observational studies of natural cirrus clouds indicate a general increase in the lidar ratio with increasing optical thickness [Chen *et al.*, 2002; Sassen and Comstock, 2001].

4.4. Discussion

The value of δ is large in young contrails and contrail cores, particularly at low ambient temperatures. These results suggest that δ tends to be high when ice crystal size is small. Individual ice crystal habits and the mixture models show δ to be weakly size dependent (Figs. 14 and 16).

As shown in Figs. 14 and 17, the highest theoretical value for faceted ice crystals included in our study is approximately 0.57. Based on theoretical scattering computations, Mishchenko and Sassen [1998] ascribed the high δ occasionally found in contrails to a dominance of very small, nearly spherical particles (spheroids or Chebyshev particles). Their calculations, with additional results from Liu and Mishchenko [2001], indicate that δ can be quite high (> 0.6) for nearly spherical particles with $D_{\text{eff}} = 2\text{--}5 \mu\text{m}$. Contrails, which show very high δ values (> 0.6) with small vertical extent (Fig. 9), may be dominated by very small, nearly spherical particles either present when the initial frozen droplets grow slowly or when ice crystals are evaporating in subsaturated ambient air. However, such small-size particles are unlikely to exist in aged contrails. Most contrails in our observation data analysis were considered to be older than ~ 2 min during which ice-supersaturation is common (Fig. 3d). Simulations by a Lagrangian particle-tracking model [Unterstrasser and Solch, 2010] suggest the mean diameter of ice crystals to be $4\text{--}10 \mu\text{m}$ at the end of the vortex phase (2 min). Using a split window remote sensing technique, Minnis *et al.* [1998] and Duda and Spinhirne [1998] found the effective diameter to be approximately $14\text{--}30 \mu\text{m}$ in young contrails and

40–90 μm in old contrails. From ground-based near-infrared spectra, *Langford et al.* [2005] suggested the effective diameter to increase from a value less than 20 μm in isolated contrails to more than 40 μm in a 1–2 km thick cirrus formed by coalescing contrails. *Karcher et al.* [2009] obtained an average effective diameter of 30–42 μm by uniformly sampling simulated contrails aged between 2 min and 4 hours. Large eddy model simulations conducted by *Unterstrasser and Gierens* [2010], using a two-moment bulk microphysics scheme, showed an increase in the extinction-weighted mean effective diameter from 10 to 40–80 μm in a time range from 5 min to 2–3 hours. Thus, a typical effective diameter in a persistent contrail is likely to be larger than 10 μm and smaller than that of cirrus clouds. These results confirm that the effective diameter of 20 μm , for an ice crystal model used in passive retrievals carried out by *Meyer et al.* [2002], *Minnis et al.* [2005], and *Palikonda et al.* [2005], was a reasonable choice, although on average, a temperature or age-dependent value may be more accurate.

One possible explanation for high δ values in contrails may be ice crystal surface roughness. In this case, δ may be low for large particle sizes (models 1 and 3 in Fig. 16b). In off-nadir observations, the average δ is about 0.44 in contrails and 0.41 in neighboring cirrus. Assuming average $D_{\text{eff}} = 10 \mu\text{m}$ in contrails and $D_{\text{eff}} = 50 \mu\text{m}$ in neighboring cirrus, the observed slight difference in δ is consistent with the theoretical predictions for model 1 with moderate surface roughness (Fig. 16b). Model 3, which includes many plates, can more easily explain the lower δ for larger D_{eff} . However, a dominance of plates is unlikely in cold air (temperature $< -40^\circ\text{C}$) where most ice crystals have columnar shapes [*Bailey and Hallett*, 2009]. If surface roughness is present, the computed lidar ratio for $D_{\text{eff}} > 30 \mu\text{m}$ exceeds 50 sr and seems too high (Fig. 17).

An alternative explanation for the lower δ values for larger particle sizes is associated with the presence of horizontally oriented plates. In the actual atmosphere, large plates are expected to align horizontally with some angular wobble. The wobble angle may depend on the particle size and shape and is estimated to be in a range of 0.3° – 2° [*Reichardt et al.*, 2002; *Sassen*, 1991]. If the wobble angle is small, significantly strong backscattering can be observed only when the lidar-pointing angle is small. For larger wobble angles, relatively weak backscattering enhancement can be observed for larger lidar-pointing angles. The lidar and depolarization ratios are expected to be

substantially reduced if a small fraction of the ice crystals are oriented horizontally. For example, *Sassen and Benson* [2001] and *Reichardt et al.* [2002] suggested the presence of 0.1–1% ice particles was enough to lower the δ value from 0.4 to 0.3. Therefore, increasing the population fraction and/or decreasing the wobble angle of the oriented plates could explain the reduction in the depolarization ratio of scattering volume. Small particles, dominant in young contrails, contrail cores, and at low temperatures, are expected to be randomly oriented. Their depolarization ratios observed by off-nadir pointing are relatively high and generally agree with the theoretical predictions for habit mixtures. As shown in Section 3, our observation results indicate slight but non-negligible influences by oriented plates, particularly in old contrails and cirrus clouds. With increasing particle sizes, the influence of the horizontally oriented plates could also increase.

5. Conclusive remarks

Combined CALIOP and MODIS observations were used to derive statistics of the physical and optical properties of persistent contrails (or contrail cirrus). Contrail locations were determined based on MODIS image analysis; and CALIOP data, collocated with the MODIS data, were analyzed for the identified contrails. Approximately 3400 persistent contrails over a region including North America, the North Atlantic Ocean, Greenland, and Europe have been analyzed. Lidar-derived optical properties were compared between contrails and the neighboring cirrus.

Based on the present analyses, statistics of some contrail properties have been obtained. The average, mid-level altitude is 10.7 km and decreases with increasing latitude. The average mid-level temperature is -54°C , and the majority of contrails are found at temperatures below -40°C , implying that homogeneous nucleation of ice crystals (i.e., droplet freezing) may be the primary mechanism for contrail formation. The average relative humidity with respect to ice (RH_{ice}) is 126 % at the mid-level, and the majority of contrails (65%) are found in moderately supersaturated air ($100\% < \text{RH}_{\text{ice}} < 150\%$). The contrail width is proportional to the square of the thickness, and

geometrically thick contrails can grow in humid environments. The average length of a continuous contrail is 264 km or longer.

The depolarization ratio (δ) is high in young contrails (age $< \sim 13$ min) and in contrail cores, but is low along the peripheries. Old contrails have smaller backscattering coefficients and lower depolarization ratios with values close to those of neighboring cirrus clouds. Furthermore, the depolarization ratio of contrails weakly depends on the lidar pointing angle compared to cirrus clouds. The weak dependence suggests that contrails are mainly composed of small, randomly oriented ice crystals with a few (but non-negligible) horizontally oriented plates. The observed depolarization ratio average and variations are generally consistent with theoretical simulations based on a mixture of non-spherical ice crystals with random orientations. To be more specific, except for very fresh contrails in the vortex phase (< 2 min), young contrails are characterized by a high concentration of small particles that are randomly oriented and exhibit relatively high depolarization ratios. Small particles can be represented by compact geometries or nearly spherical particles. Relatively thin contrails occasionally exhibit strong depolarization ($\delta > 0.6$) that cannot be explained by faceted ice crystals (plates or columns). A possible explanation may be that very small ($D_{\text{eff}} = 2\text{--}5 \mu\text{m}$), nearly spherical (or ellipsoidal) particles dominate when particles slowly grow/evaporate in ambient air with relative humidity close to 100%.

Most contrails are optically thin. The average optical thickness (τ) of contrails is about 0.19 with large variability, and the median is approximately 0.14, according to off-nadir observations. About 34% of contrail columns have $\tau < 0.1$. Thick contrails with $\tau > 0.5$ count for only 5% of off-nadir and 10% of quasi-nadir observations.

As shown in Section 4, the lidar ratio is very sensitive to the ice particle size, shape, and surface roughness (or irregularity of particle shape). The cirrus lidar ratio dependence on optical thickness and temperature [*Chen et al.*, 2002; *Sassen and Comstock*, 2001] suggests a linkage between microphysical properties and meteorological conditions. At this point, our understanding of backscattering properties for contrails and contrail cirrus is still limited, particularly regarding particle surface roughness, irregularity, air-bubble-containing ice crystals, and edge roundness of evaporating ice crystals [*Korolev and Isaac*, 2003; *Korolev et al.*, 2000; *Nelson*, 1998; *Nousiainen and*

McFarquhar, 2004; Shcherbakov et al., 2006]. Continued effort from the atmospheric research community is needed in this area.

Acknowledgements.

This work was supported by the Aviation Climate Change Research Initiative (ACCRI) sponsored by the Federal Aviation Administration (FAA) under contracts DTRT57-10-C-10016 and DTRT57-10-X-70020. The authors thank Dr. Rangasayi Halthore and Dr. S. Daniel Jacob from the FAA for their overseeing the project progress and for their guidance and encouragements. The CALIPSO data were obtained from the NASA Langley Research Center Atmospheric Science Data Center. The MODIS data were obtained from NASA/GSFC, MODIS Rapid Response System and the Level 1 and Atmosphere Archive and Distribution System (LAADS).

References

- Atlas, D., and Z. E. Wang (2010), Contrails of Small and Very Large Optical Depth, *J. Atmos. Sci.*, *67*(9), 3065-3073.
- Atlas, D., Z. Wang, and D. P. Duda (2006), Contrails to cirrus - Morphology, microphysics, and radiative properties, *J. Appl. Meteorol. Clim.*, *45*(1), 5-19.
- Baker, B. A., and R. P. Lawson (2006), In situ observations of the microphysical properties of wave, cirrus, and anvil clouds. Part I: Wave clouds, *J. Atmos. Sci.*, *63*(12), 3160-3185.
- Baran, A. J. (2009), A review of the light scattering properties of cirrus, *J. Quant. Spectrosc. Radiat. Transfer* *110*(14-16), 1239-1260.
- Baum, B. A., A. J. Heymsfield, P. Yang, and S. T. Bedka (2005), Bulk scattering properties for the remote sensing of ice clouds. Part I: Microphysical data and models, *J. Appl. Meteor.*, *44*(12), 1885-1895.
- Baumgardner, D., and B. E. Gandrud (1998), A comparison of the microphysical and optical properties of particles in an aircraft contrail and mountain wave cloud, *Geophys. Res. Lett.*, *25*(8), 1129-1132.
- Betancor-Gothe, M., and H. Grassl (1993), Satellite remote-sensing of the optical depth and mean crystal size of thin cirrus and contrails, *Theor. Appl. Climatol.*, *48*(2-3), 101-113.
- Bi, L., P. Yang, G. W. Kattawar, B. A. Baum, Y. X. Hu, D. M. Winker, R. S. Brock, and J. Q. Lu (2009), Simulation of the color ratio associated with the backscattering of radiation by ice crystals at 0.532 and 1.064 μm wavelengths, *J. Geophys. Res.*, *114*, D00H08, doi: 10.1029/2009JD011759.
- Burkhardt, U., and B. Karcher (2009), Process-based simulation of contrail cirrus in a global climate model, *J. Geophys. Res.*, *114*, D16201, doi:10.1029/2008JD011491.
- Chen, W. N., C. W. Chiang, and J. B. Nee (2002), Lidar ratio and depolarization ratio for cirrus clouds, *Appl. Opt.*, *41*(30), 6470-6476.
- Cho, H. M., P. Yang, G. W. Kattawar, S. L. Nasiri, Y. X. Hu, P. Minnis, C. Trepte, and D. Winker (2008), Depolarization ratio and attenuated backscatter for nine cloud types: Analyses based on collocated CALIPSO lidar and MODIS measurements, *Opt Express*, *16*(6), 3931-3948.
- Del Guasta, M., and K. Niranjana (2001), Observation of low-depolarization contrails at Florence (Italy) using a 532-1064 nm polarization LIDAR, *Geophys. Res. Lett.*, *28*(21), 4067-4070.

- Duda, D. P., J. D. Spinhirne, and V. D. Hart (1998), Retrieval of contrail microphysical properties during SUCCESS by the split-window method, *Geophys. Res. Lett.*, 25(8), 1149-1152.
- Febvre, G., J. F. Gayet, A. Minikin, H. Schlager, V. Shcherbakov, O. Jourdan, R. Busen, M. Fiebig, B. Karcher, and U. Schumann (2009), On optical and microphysical characteristics of contrails and cirrus, *J. Geophys. Res.*, 114, D02204, doi:02210.01029/02008JD010184.
- Foot, J. S. (1988), Some observations of the optical properties of clouds. II: Cirrus, *Q. J. R. Meteorol. Soc.*, 114(479), 145-164.
- Freudenthaler, V., F. Homburg, and H. Jager (1995), Contrail observations by ground-based scanning lidar: Cross-sectional growth, *Geophys. Res. Lett.*, 22(24), 3501-3504.
- Freudenthaler, V., F. Homburg, and H. Jager (1996), Optical parameters of contrails from lidar measurements: Linear depolarization, *Geophys. Res. Lett.*, 23(25), 3715-3718.
- Gallagher, M. W., P. J. Connolly, J. Whiteway, D. Figueras-Nieto, M. Flynn, T. W. Choulaton, K. N. Bower, C. Cook, R. Busen, and J. Hacker (2005), An overview of the microphysical structure of cirrus clouds observed during EMERALD-1, *Q. J. R. Meteorol. Soc.*, 131(607), 1143-1169.
- Gayet, J. F., G. Febvre, G. Brogniez, H. Chepfer, W. Renger, and P. Wendling (1996), Microphysical and optical properties of cirrus and contrails: Cloud field study on 13 October 1989, *J. Atmos. Sci.*, 53(1), 126-138.
- Gayet, J. F., F. Auriol, S. Oshchepkov, F. Schroder, C. Durore, G. Febvre, J. F. Fournol, O. Crepel, P. Personne, and D. Daugereon (1998), In situ measurements of the scattering phase function of stratocumulus, contrails and cirrus, *Geophys. Res. Lett.*, 25(7), 971-974.
- Goodman, J., R. F. Pueschel, E. J. Jensen, S. Verma, G. V. Ferry, S. D. Howard, S. A. Kinne, and D. Baumgardner (1998), Shape and size of contrails ice particles, *Geophys. Res. Lett.*, 25(9), 1327-1330.
- Heymsfield, A., and G. M. McFarquhar (2002), Mid latitude and tropical cirrus microphysical properties, in *Cirrus*, edited by D. K. Lynch, K. Sassen, D. O. Starr and G. L. Stephens, pp. 78-101, Oxford Univ. .
- Heymsfield, A., D. Baumgardner, P. DeMott, P. Forster, K. Gierens, and B. Karcher (2010), Contrail Microphysics, *Bull. Amer. Meteor. Soc.*, 91(4), 465-472.
- Heymsfield, A. J., R. P. Lawson, and G. W. Sachse (1998), Growth of ice crystals in a precipitating contrail, *Geophys. Res. Lett.*, 25(9), 1335-1338.
- Hostetler, C. A., Z. Liu, J. A. Reagan, M. A. Vaughan, D. M. Winker, M. T. Osborn, W. H. Hunt, K. A. Powell, and C. R. Trepte (2005), CALIPSO algorithm theoretical basis

document: PC - SCI - 201, edited, (Available online at http://www-calipso.larc.nasa.gov/resources/project_documentation.php).

Hu, Y. X., M. Vaughan, Z. Y. Liu, B. Lin, P. Yang, D. Flittner, B. Hunt, R. Kuehn, J. P. Huang, D. Wu, S. Rodier, K. Powell, C. Trepte, and D. Winker (2007), The depolarization - attenuated backscatter relation: CALIPSO lidar measurements vs. theory, *Opt Express*, 15(9), 5327-5332.

Immler, F., and O. Schrems (2002), LIDAR measurements of cirrus clouds in the northern and southern midlatitudes during INCA (55°N, 53°S): A comparative study, *Geophys. Res. Lett.*, 29(16), 1809, 1810.1029/2002GL015077.

Jensen, E. J., A. S. Ackerman, D. E. Stevens, O. B. Toon, and P. Minnis (1998), Spreading and growth of contrails in a sheared environment, *J. Geophys. Res.*, 103(D24), 31557-31567.

Karcher, B., U. Burkhardt, S. Unterstrasser, and P. Minnis (2009), Factors controlling contrail cirrus optical depth, *Atmos. Chem. Phys.*, 9(16), 6227-6254.

Karcher, B., U. Burkhardt, M. Ponater, and C. Fromming (2010), Importance of representing optical depth variability for estimates of global line-shaped contrail radiative forcing, *Proc. of the National Academy of Sciences of the United States of America*, 107(45), 19181-19184.

Knollenb, R. G. (1972), Measurements of growth of ice budget in a persisting contrail, *J. Atmos. Sci.*, 29(7), 1367-1374.

Korolev, A., and G. Isaac (2003), Roundness and aspect ratio of particles in ice clouds, *J. Atmos. Sci.*, 60(15), 1795-1808.

Korolev, A., G. A. Isaac, and J. Hallett (2000), Ice particle habits in stratiform clouds, *Q. J. R. Meteorol. Soc.*, 126(569), 2873-2902.

Langford, A. O., R. W. Portmann, J. S. Daniel, H. L. Miller, C. S. Eubank, S. Solomon, and E. G. Dutton (2005), Retrieval of ice crystal effective diameters from ground-based near-infrared spectra of optically thin cirrus, *J. Geophys. Res.*, 110(D22), D22201, doi:22210.21029/22005JD005761.

Lawson, R. P., A. J. Heymsfield, S. M. Aulenbach, and T. L. Jensen (1998), Shapes, sizes and light scattering properties of ice crystals in cirrus and a persistent contrail during SUCCESS, *Geophys. Res. Lett.*, 25(9), 1331-1334.

Lawson, R. P., B. Baker, B. Pilon, and Q. X. Mo (2006), In situ observations of the microphysical properties of wave, cirrus, and anvil clouds. Part II: Cirrus clouds, *J. Atmos. Sci.*, 63(12), 3186-3203.

- Lee, D. S., D. W. Fahey, P. M. Forster, P. J. Newton, R. C. N. Wit, L. L. Lim, B. Owen, and R. Sausen (2009), Aviation and global climate change in the 21st century, *Atmos. Environ.*, *43*(22-23), 3520-3537.
- Liou, K. N., P. Yang, Y. Takano, K. Sassen, T. Charlock, and W. Arnott (1998), On the radiative properties of contrail cirrus, *Geophys. Res. Lett.*, *25*(8), 1161-1164.
- Liu, L., and M. I. Mishchenko (2001), Constraints on PSC particle microphysics derived from lidar observations, *J. Quant. Spectrosc. Radiat. Transfer*, *70*(4-6), 817-831.
- Marquart, S., M. Ponater, F. Mager, and R. Sausen (2003), Future development of contrail cover, optical depth, and radiative forcing: Impacts of increasing air traffic and climate change, *J. Clim.*, *16*(17), 2890-2904.
- Meerkotter, R., U. Schumann, D. R. Doelling, P. Minnis, T. Nakajima, and Y. Tsushima (1999), Radiative forcing by contrails, *Ann Geophys*, *17*(8), 1080-1094.
- Meyer, R., H. Mannstein, R. Meerkotter, U. Schumann, and P. Wendling (2002), Regional radiative forcing by line-shaped contrails derived from satellite data, *J. Geophys. Res.*, *107*(D10), 4104, doi: 4110.1029/2001JD000426.
- Minnis, P., J. K. Ayers, R. Palikonda, and D. Phan (2004), Contrails, cirrus trends, and climate, *J. Clim.*, *17*(8), 1671-1685.
- Minnis, P., R. Palikonda, B. J. Walter, J. K. Ayers, and H. Mannstein (2005), Contrail properties over the eastern North Pacific from AVHRR data, *Meteor. Z.*, *14*(4), 515-523.
- Minnis, P., D. F. Young, D. P. Garber, L. Nguyen, W. L. Smith, and R. Palikonda (1998), Transformation of contrails into cirrus during SUCCESS, *Geophys. Res. Lett.*, *25*(8), 1157-1160.
- Mishchenko, M. I., and K. Sassen (1998), Depolarization of lidar returns by small ice crystals: An application to contrails, *Geophys. Res. Lett.*, *25*(3), 309-312.
- Nelson, J. (1998), Sublimation of ice crystals, *J. Atmos. Sci.*, *55*(5), 910-919.
- Nousiainen, T., and G. M. McFarquhar (2004), Light scattering by quasi-spherical ice crystals, *J. Atmos. Sci.*, *61*(18), 2229-2248.
- Palikonda, R., P. Minnis, D. P. Duda, and H. Mannstein (2005), Contrail coverage derived from 2001 AVHRR data over the continental United States of America and surrounding areas, *Meteorol. Z.*, *14*(4), 525-536.
- Petzold, A., R. Busen, F. P. Schroder, R. Baumann, M. Kuhn, J. Strom, D. E. Hagen, P. D. Whitefield, D. Baumgardner, F. Arnold, S. Borrmann, and U. Schumann (1997), Near-field measurements on contrail properties from fuels with different sulfur content, *J. Geophys. Res.*, *102*(D25), 29867-29880.

- Poellot, M. R., W. P. Arnott, and J. Hallett (1999), In situ observations of contrail microphysics and implications for their radiative impact, *J. Geophys. Res.*, *104*(D10), 12077-12084.
- Ponater, M., S. Brinkop, R. Sausen, and U. Schumann (1996), Simulating the global atmospheric response to aircraft water vapour emissions and contrails: A first approach using a GCM, *Ann Geophys*, *14*(9), 941-960.
- Rap, A., P. M. Forster, J. M. Haywood, A. Jones, and O. Boucher (2010), Estimating the climate impact of linear contrails using the UK Met Office climate model, *Geophys. Res. Lett.*, *37*, L20703, doi:20710.21029/22010GL045161.
- Reichardt, J., S. Reichardt, M. Hess, and T. J. McGee (2002), Correlations among the optical properties of cirrus-cloud particles: Microphysical interpretation, *J. Geophys. Res.*, *107*(D21), 4562, doi:4510.1029/2002JD002589.
- Sakai, T., T. Nagai, M. Nakazato, Y. Mano, and T. Matsumura (2003), Ice clouds and Asian dust studied with lidar measurements of particle extinction-to-backscatter ratio, particle depolarization, and water-vapor mixing ratio over Tsukuba, *Appl. Opt.*, *42*(36), 7103-7116.
- Sassen, K. (1979), Iridescence in an aircraft contrail, *J. Opt. Soc. Am.*, *69*(8), 1080-1083.
- Sassen, K. (1991), The polarization lidar technique for cloud research: a review and current assessment, *Bull. Amer. Meteor. Soc.*, *72*(12), 1848-1866.
- Sassen, K. (1997), Contrail-cirrus and their potential for regional climate change, *Bull. Amer. Meteor. Soc.*, *78*(9), 1885-1903.
- Sassen, K., and C. Y. Hsueh (1998), Contrail properties derived from high-resolution polarization lidar studies during SUCCESS, *Geophys. Res. Lett.*, *25*(8), 1165-1168.
- Sassen, K., and S. Benson (2001), A midlatitude cirrus cloud climatology from the facility for atmospheric remote sensing. Part II: Microphysical properties derived from lidar depolarization, *J. Atmos. Sci.*, *58*(15), 2103-2112.
- Sassen, K., and J. M. Comstock (2001), A midlatitude cirrus cloud climatology from the facility for atmospheric remote sensing. Part III: Radiative properties, *J. Atmos. Sci.*, *58*(15), 2113-2127.
- Sassen, K., and J. Zhu (2009), A global survey of CALIPSO linear depolarization ratios in ice clouds: Initial findings, *J. Geophys. Res.*, *114*, D00H07, doi:10.1029/2009JD012279.
- Schroder, F., B. Karcher, C. Durore, J. Strom, A. Petzold, J. F. Gayet, B. Strauss, P. Wendling, and S. Borrmann (2000), On the transition of contrails into cirrus clouds, *J. Atmos. Sci.*, *57*(4), 464-480.

Schumann, U. (2002), Contrail cirrus, in *Cirrus*, edited by D. K. Lynch, K. Sassen, D. O. Starr and G. L. Stephens, pp. 231-255, Oxford Univ.

Schumann, U., B. Mayer, K. Gierens, S. Unterstrasser, P. Jessberger, A. Petzold, C. Voigt, and J. F. Gayet (2010), Effective radius of ice particles in cirrus and contrails, *J. Atmos. Sci.*, *in press*.

Shcherbakov, V., J. F. Gayet, B. Baker, and P. Lawson (2006), Light scattering by single natural ice crystals, *J. Atmos. Sci.*, *63*(5), 1513-1525.

Spinhirne, J. D., W. D. Hart, and D. P. Duda (1998), Evolution of the morphology and microphysics of contrail cirrus from airborne remote sensing, *Geophys. Res. Lett.*, *25*(8), 1153-1156.

Sussmann, R. (1997), Optical properties of contrail-induced cirrus: Discussion of unusual halo phenomena, *Appl. Opt.*, *36*(18), 4195-4201.

Sussmann, R., and K. M. Gierens (1999), Lidar and numerical studies on the different evolution of vortex pair and secondary wake in young contrails, *J. Geophys. Res.*, *104*(D2), 2131-2142.

Sussmann, R., and K. M. Gierens (2001), Differences in early contrail evolution of two-engine versus four-engine aircraft: Lidar measurements and numerical simulations, *J. Geophys. Res.*, *106*(D5), 4899-4911.

Unterstrasser, S., and K. Gierens (2010), Numerical simulations of contrail-to-cirrus transition. Part I: An extensive parametric study, *Atmos. Chem. Phys.*, *10*(4), 2017-2036.

Unterstrasser, S., and I. Solch (2010), Study of contrail microphysics in the vortex phase with a Lagrangian particle tracking model, *Atmos. Chem. Phys.*, *10*(20), 10003-10015.

Vaughan, M. A., Z. Y. Liu, M. J. McGill, Y. X. Hu, and M. D. Obland (2010), On the spectral dependence of backscatter from cirrus clouds: Assessing CALIOP's 1064 nm calibration assumptions using cloud physics lidar measurements, *J. Geophys. Res.*, *115*, D14206, doi:14210.11029/12009JD013086.

Whiteway, J., C. Cook, M. Gallagher, T. Choullarton, J. Harries, P. Connolly, R. Busen, K. Bower, M. Flynn, P. May, R. Aspey, and J. Hacker (2004), Anatomy of cirrus clouds: Results from the Emerald airborne campaigns, *Geophys. Res. Lett.*, *31*(24), L24102, doi:24110.21029/22004GL021201.

Xie, Y., P. Yang, G. W. Kattawar, P. Minnis, and Y. X. Hu (2009), Effect of the inhomogeneity of ice crystals on retrieving ice cloud optical thickness and effective particle size, *J. Geophys. Res.*, *114*, D11203, doi:11210.11029/12008JD011216.

Yang, P., and K. N. Liou (1996), Geometric-optics-integral-equation method for light scattering by nonspherical ice crystals, *Appl. Opt.*, *35*(33), 6568-6584.

Yang, P., and K. N. Liou (1998), Single scattering properties of complex ice crystals in terrestrial atmosphere, *Contrib. Atmos. Phys.*, *71*, 223-248.

Yang, P., K. N. Liou, K. Wyser, and D. Mitchell (2000), Parameterization of the scattering and absorption properties of individual ice crystals, *J. Geophys. Res.*, *105*(D4), 4699-4718.

Yang, P., G. Hong, G. W. Kattawar, P. Minnis, and Y. X. Hu (2008), Uncertainties associated with the surface texture of ice particles in satellite-based retrieval of cirrus clouds. Part II: Effect of particle surface roughness on retrieved cloud optical thickness and effective particle size, *IEEE Transactions on Geoscience and Remote Sensing* *46*(7), 1948-1957.

Yang, P., G. Hong, A. E. Dessler, S. S. C. Ou, K. N. Liou, P. Minnis, and Harshvardhan (2010), Contrails and induced cirrus optics and radiation, *Bull. Amer. Meteor. Soc.*, *91*(4), 473-478.

Yang, P., H. L. Wei, H. L. Huang, B. A. Baum, Y. X. Hu, G. W. Kattawar, M. I. Mishchenko, and Q. Fu (2005), Scattering and absorption property database for nonspherical ice particles in the near- through far-infrared spectral region, *Appl. Opt.*, *44*(26), 5512-5523.

You, Y., G. W. Kattawar, P. Yang, Y. X. Hu, and B. A. Baum (2006), Sensitivity of depolarized lidar signals to cloud and aerosol particle properties, *J. Quant. Spectrosc. Radiat. Transfer*, *100*(1-3), 470-482.

Tables and figures

Table 1. Summary statistics of geographical, geometrical, and meteorological properties of contrails analyzed in this study. Averages are shown with standard deviations in brackets. RH_{ice} denotes relative humidity with respect to ice.

Table 2. Summary statistics of lidar-derived optical properties for contrails and the neighboring cirrus clouds: Depolarization ratio (δ), color ratio (χ), total backscattering coefficient at a wavelength of 532 nm (β_{532}), and optical thickness at 532 nm (τ_{532}). Averages are shown with standard deviations in brackets.

Table 3. Same as Table 2 but for the three contrail types.

Fig. 1. Upper: An image of MODIS brightness temperature difference (BTD) between 11 and 12- μ m channels over the Northeast Pacific 11 January 2009. Cyan line denotes the locations of MODIS-CALIOP collocated pixels. Magenta line segments denote contrails detected by manual inspection. Middle and lower: CALIOP profiles of attenuated total (middle) and perpendicular (lower) backscattering coefficients ($\text{km}^{-1} \text{sr}^{-1}$) at 532 nm wavelength corresponding to the scene in the MODIS image. Red vertical lines denote contrail locations detected by MODIS image analysis. Only cloudy cross sectional elements are plotted.

Fig. 2. Geographical locations of contrails analyzed in this study. Each single cross mark denotes a contrail location identified by MODIS and CALIOP data analysis.

Fig. 3. (a) Scatter plot of mid-level altitude and latitude. (b) Histogram of relative humidity with respect to ice at mid-level within contrail. (c) Scatter plot of geometrical thickness and width. (d) Histogram of length. Least-square fits of a line and a power law curve are superimposed in (a) and (c), respectively.

Fig. 4. Average geometrical thickness as a function of width and relative humidity with respect to ice.

Fig. 5. Averages at 532 nm, (a) backscattering coefficients, (b) depolarization ratios, (c) color ratios, and (d) optical thicknesses. Y, M, and O denote young, mature, and old contrails. P and C denote contrail peripheries and cores. Averages for all contrails and neighboring cirrus clouds are respectively denoted by A and Ci. Averages were computed for the years 2007 and 2009 for which CALIOP had different off-nadir angles of 0.3° and 3° .

Fig. 6. Two-dimensional frequency distributions of depolarization ratio and total backscattering coefficient at 532 nm of contrails and neighboring cirrus clouds for; (a) off-nadir measurements in 2007, and (b) quasi-nadir measurements in 2009. Contour lines are drawn for equally spaced frequency values.

Fig. 7. Same as Fig. 6 but for comparison of contrail cores and peripheries.

Fig. 8. Same as Fig. 6 but for color ratio and total backscattering coefficient at 532 nm.

Fig. 9. Scatter plots of (a) the depolarization ratio and altitude, (b) temperature, and (c) geometrical thickness for contrails, and (d) the depolarization ratio and temperature for neighboring cirrus clouds. Least-square lines are superimposed.

Fig. 10. Average depolarization ratio as a function of temperature and geometrical thickness obtained from measurements in (a) 2007 and (b) 2009.

Fig. 11. Histograms of contrail optical thickness at a wavelength of 532 nm obtained from measurements in (a) 2007 and (b) 2009.

Fig. 12. The optical thickness dependence on temperature and relative humidity with respect to ice. (a) Scatter plot of optical thickness at 532 nm and temperature. (b) Scatter

plot of optical thickness and relative humidity with respect to ice. (c, d) Average optical thickness at 532 nm as a function of temperature and relative humidity with respect to ice for years (a) 2007 and (b) 2009. Least-square lines are superimposed in (a) and (b).

Fig. 13. Relationship between the shape parameter (α) and the scale parameter (ν) of the PSD represented by the Gamma distribution. Data obtained from in-situ measurements presented in *Baum et al.* [2005] (denoted by B05) are shown by dots. Data computed from previous in-situ measurements presented in the literature are shown by squares for cirrus clouds and triangles for contrails. The solid line denotes a least-square fit and the dashed lines denote equations with twofold $\alpha + 2$ smaller or larger values than the least-square fit.

Fig. 14. Derived from IGOM calculations, (a,b) the theoretical lidar ratio, (c,d) depolarization ratio at a wavelength of 532 nm, and (e,f) color ratio as functions of the effective particle diameter for hexagonal particle polydispersions with various aspect ratios ($2a/L$). Random particle orientation is assumed. Results are shown for smooth particles ($\sigma = 0$) (a,c,e) and particles with moderate surface roughness ($\sigma = 0.1$) (b,d,f).

Fig. 15. Ice crystal habit fractions, as functions of the maximum dimension, for habit mixture models 1–3. Considered ice crystal habits include droxtals (DRX), solid/hollow columns (SCOL/HCOL), plates (PLA), solid/hollow bullet rosettes (SBUL/HBUL), aggregates (AGG), and irregulars (IRR).

Fig. 16. Theoretical depolarization ratios at a wavelength of 532 nm as functions of effective diameter for habit mixture models (a) with and (b) without surface roughness.

Fig. 17. Theoretical relationships between depolarization ratio and lidar ratio for (a) ice particle habits and (b) for habit mixture models. For each habit or habit mixture model, three points correspond to effective diameters of 10, 20, and 50 μm . A sphere habit is denoted by SPH, and other habit notations are the same as in Fig. 15. Superimposed rectangles denote ranges of depolarization ratio for contrails obtained from CALIOP data

analysis in this study (average plus/minus one standard deviation) and a possible range of lidar ratio obtained in previous lidar measurements for contrail and optically thin natural cirrus cloud.

Table 1. Summary statistics of geographical, geometrical, and meteorological properties of contrails analyzed in this study. Averages are shown with standard deviations in brackets. RH_{ice} denotes relative humidity with respect to ice.

Latitude (° N)	51.9 (10.3)
Altitude (km)	10.7 (1.0)
Width (km)	6.5 (4.8)
Thickness (km)	0.67 (0.32)
Length (km)	264 (294)
Temperature (°C)	-53.4 (5.3)
RH_{ice} (%)	126 (26)

Table 2. Summary statistics of lidar-derived optical properties for contrails and the neighboring cirrus clouds: Depolarization ratio (δ), color ratio (χ), total backscattering coefficient at a wavelength of 532 nm (β_{532}), and optical thickness at 532 nm (τ_{532}). Averages are shown with standard deviations in brackets.

	Contrails	Neighboring Cirrus Clouds
Quasi-Nadir Observations -2007-		
β_{532} (/km/sr)	0.0232 (0.0170)	0.0138 (0.0076)
δ	0.393 (0.127)	0.319 (0.085)
χ	0.903 (0.159)	0.884 (0.100)
τ_{532}	0.240 (0.193)	-
Number of cases	1484	1425
Off-Nadir Observations -2009-		
β_{532} (/km/sr)	0.0191 (0.0145)	0.0102 (0.0053)
δ	0.439 (0.092)	0.409 (0.052)
χ	0.982 (0.143)	0.974 (0.094)
τ_{532}	0.187 (0.152)	-
Number of cases	1904	1738

Table 3. Same as Table 2 but for the three contrail types.

	Young Contrails	Mature Contrails	Old Contrails
Quasi-Nadir Observations -2007-			
β_{532} (/km/sr)	0.0270 (0.0203)	0.0242 (0.0167)	0.0174 (0.0112)
δ	0.410 (0.128)	0.392 (0.130)	0.377 (0.120)
χ	0.882 (0.173)	0.903 (0.160)	0.926 (0.138)
T_{532}	0.253 (0.228)	0.260 (0.209)	0.220 (0.163)
Number of cases	422	664	398
Off-Nadir Observations -2009-			
β_{532} (/km/sr)	0.0258 (0.0169)	0.0196 (0.0137)	0.0142 (0.0125)
δ	0.446 (0.105)	0.439 (0.092)	0.435 (0.084)
χ	0.939 (0.136)	0.984 (0.151)	1.004 (0.123)
τ_{532}	0.228 (0.171)	0.205 (0.175)	0.163 (0.120)
Number of cases	333	1026	545
Geometrical Properties -2007 & 2009-			
Width (km)	2.5 (0.6)	5.1 (1.6)	12.3 (5.2)
Thickness (km)	0.48 (0.19)	0.64 (0.27)	0.87 (0.38)
Length (km)	205 (240)	260 (299)	321 (312)

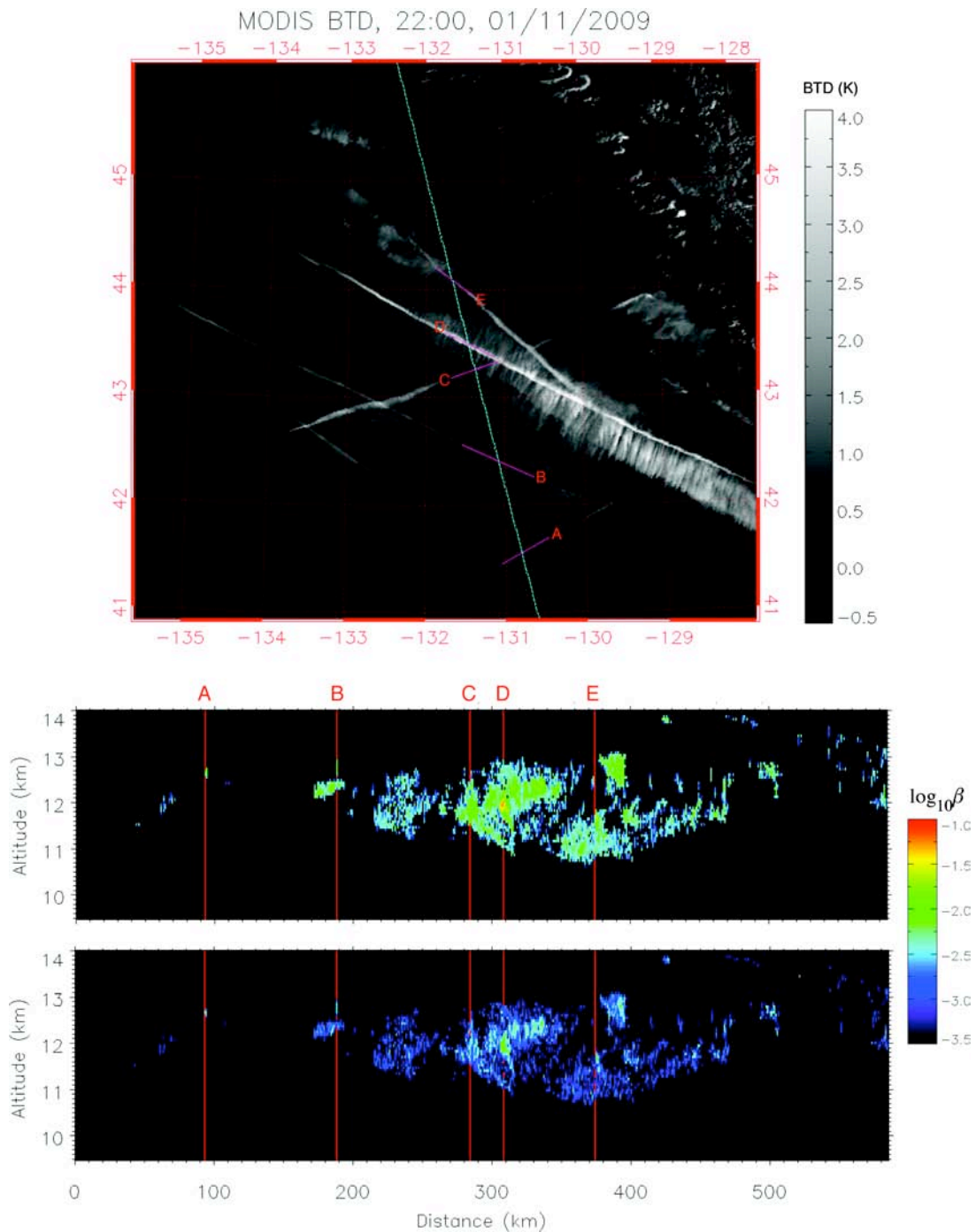


Fig. 1. Upper: An image of MODIS brightness temperature difference (BTD) between 11 and 12- μm channels over the Northeast Pacific 11 January 2009. Cyan line denotes the locations of MODIS-CALIOP collocated pixels. Magenta line segments denote contrails detected by manual inspection. Middle and lower: CALIOP profiles of attenuated total (middle) and perpendicular (lower) backscattering coefficients ($\text{km}^{-1} \text{sr}^{-1}$) at 532 nm

wavelength corresponding to the scene in the MODIS image. Red vertical lines denote contrail locations detected by MODIS image analysis. Only cloudy cross sectional elements are plotted.

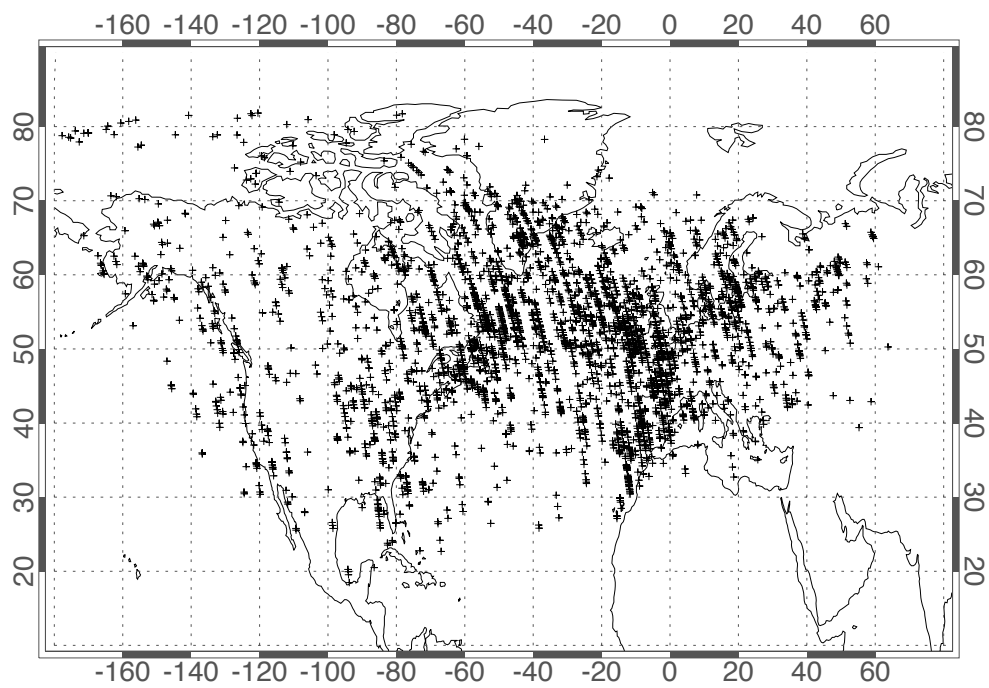


Fig. 2. Geographical locations of contrails analyzed in this study. Each single cross mark denotes a contrail location identified by MODIS and CALIOP data analysis.

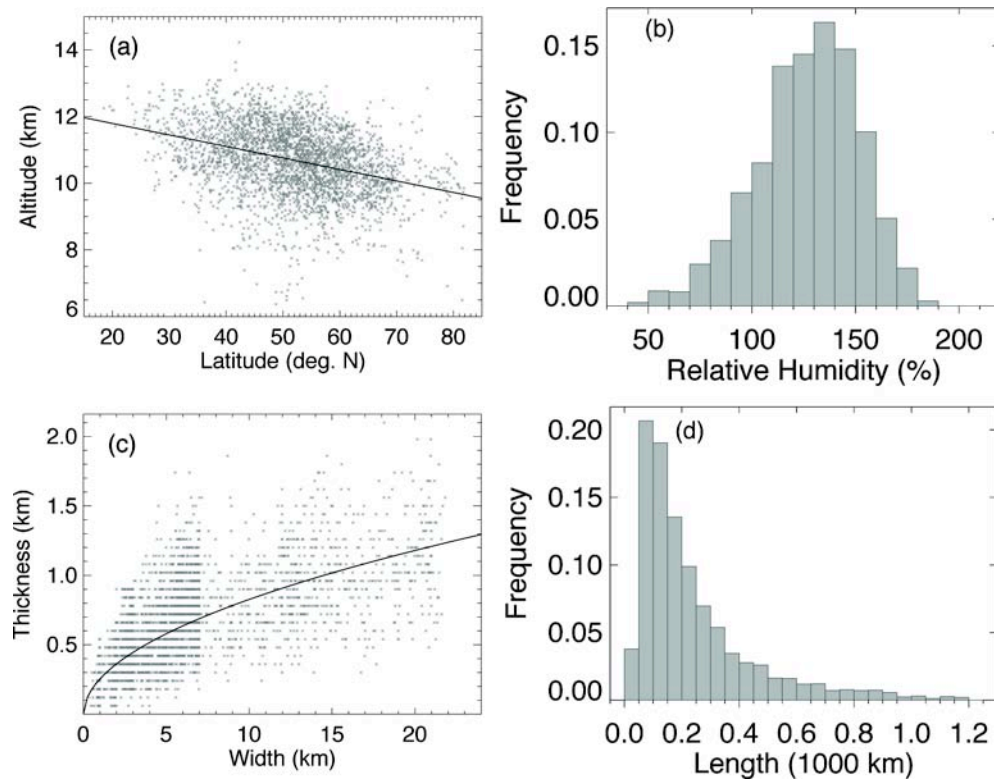


Fig. 3. (a) Scatter plot of mid-level altitude and latitude. (b) Histogram of relative humidity with respect to ice at mid-level within contrail. (c) Scatter plot of geometrical thickness and width. (d) Histogram of length. Least-square fits of a line and a power law curve are superimposed in (a) and (c), respectively.

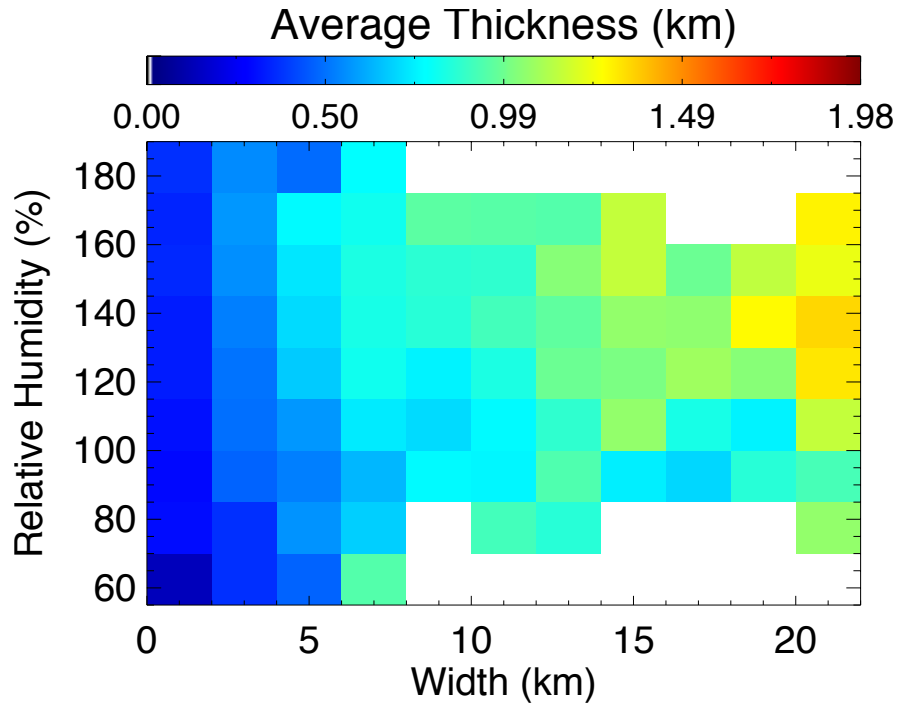


Fig. 4. Average geometrical thickness as a function of width and relative humidity with respect to ice.

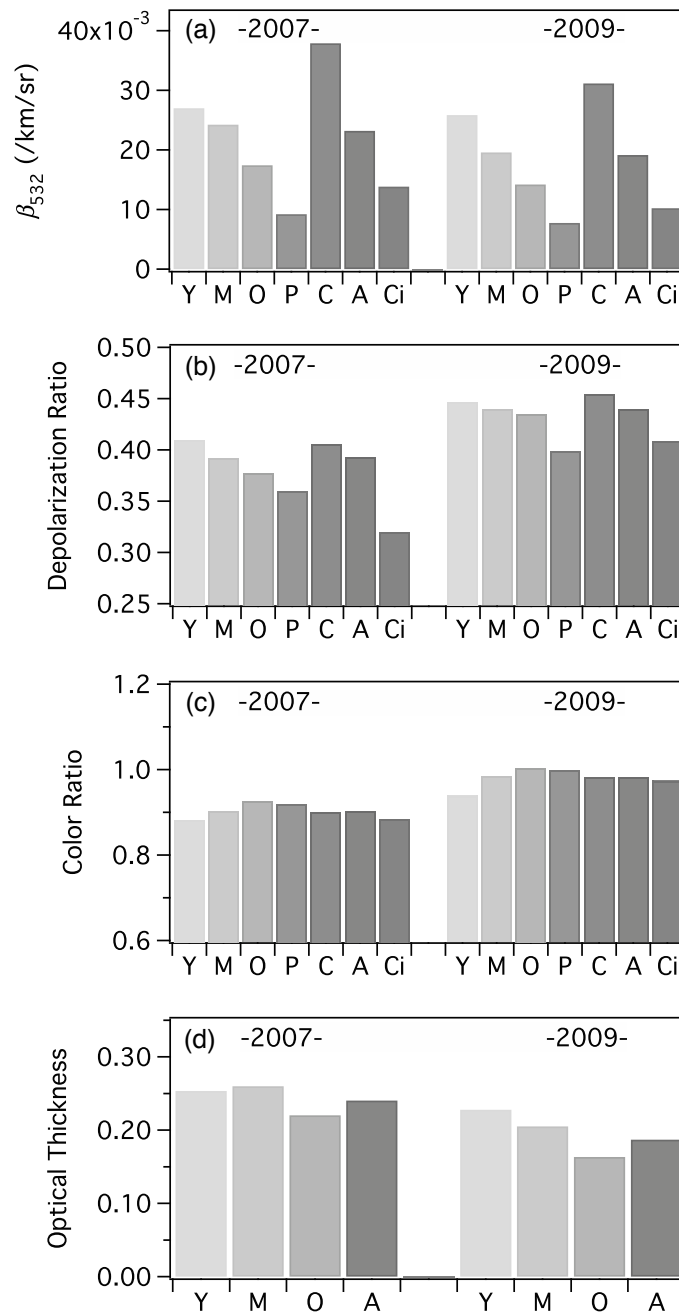


Fig. 5. Averages at 532 nm, (a) backscattering coefficients, (b) depolarization ratios, (c) color ratios, and (d) optical thicknesses. Y, M, and O denote young, mature, and old contrails. P and C denote contrail peripheries and cores. Averages for all contrails and neighboring cirrus clouds are respectively denoted by A and Ci. Averages were computed for the years 2007 and 2009 for which CALIOP had different off-nadir angles of 0.3° and 3° .

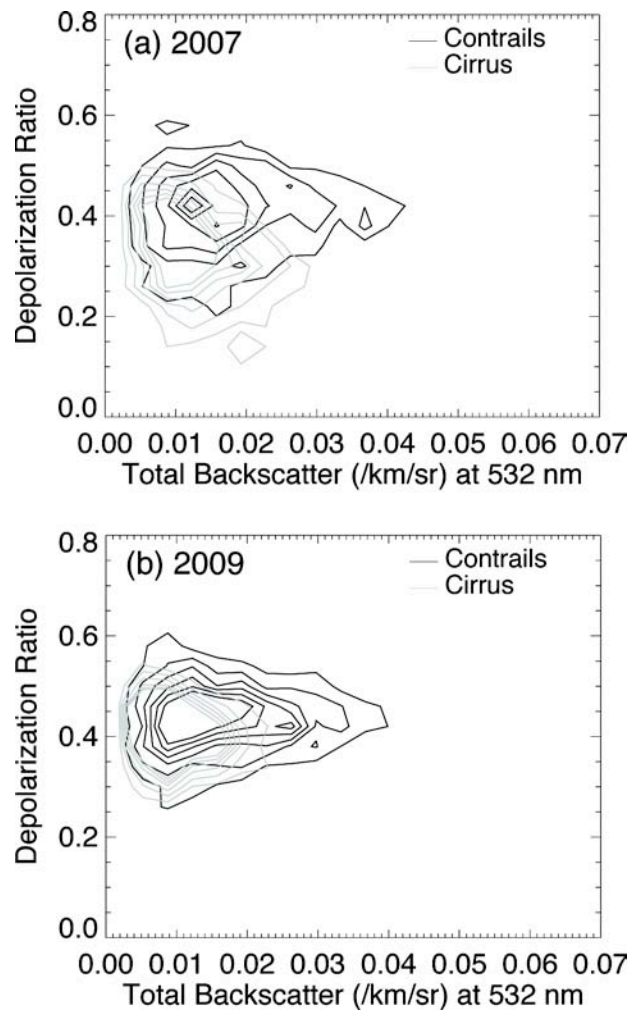


Fig. 6. Two-dimensional frequency distributions of depolarization ratio and total backscattering coefficient at 532 nm of contrails and neighboring cirrus clouds for; (a) off-nadir measurements in 2007, and (b) quasi-nadir measurements in 2009. Contour lines are drawn for equally spaced frequency values.

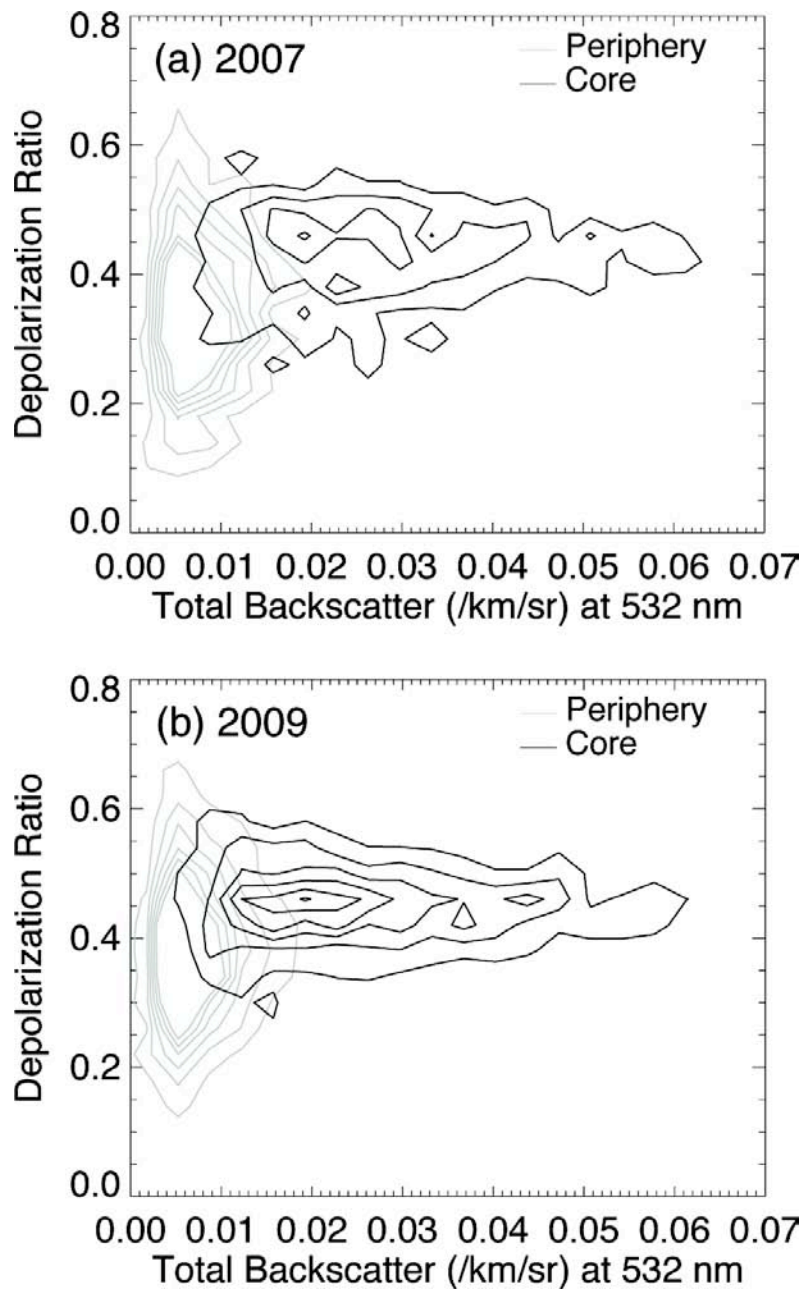


Fig. 7. Same as Fig. 6 but for comparison of contrail cores and peripheries.

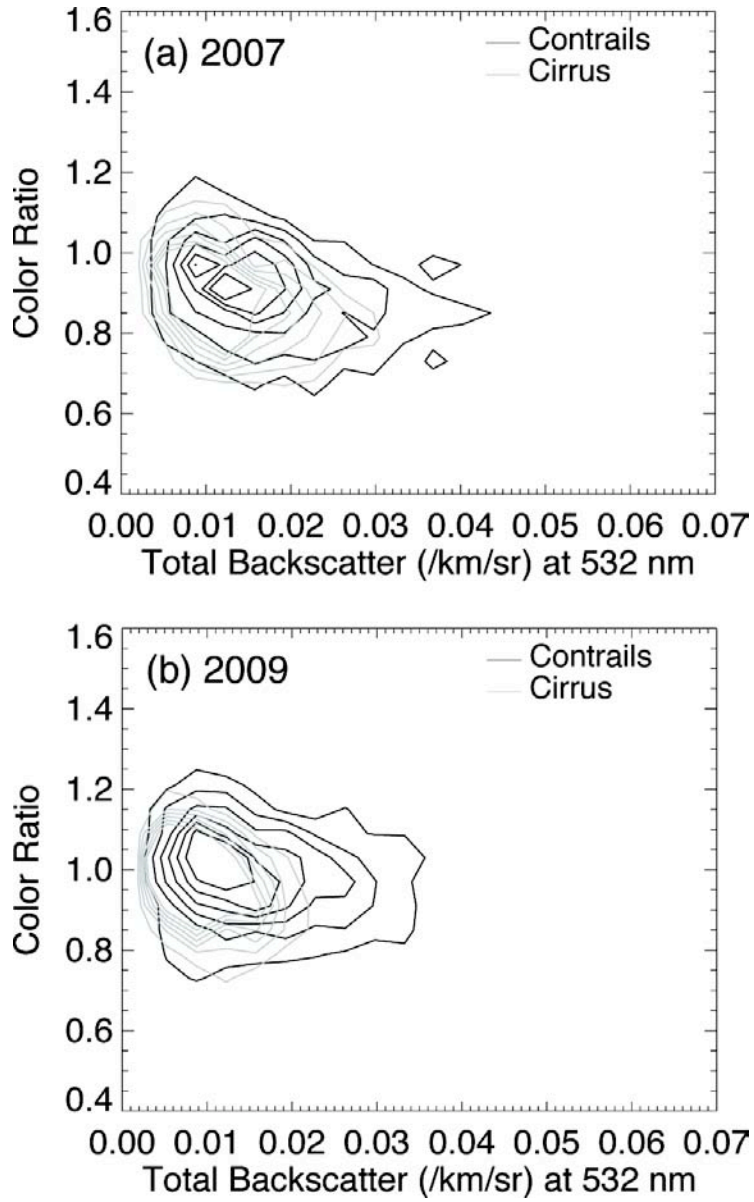


Fig. 8. Same as Fig. 6 but for color ratio and total backscattering coefficient at 532 nm.

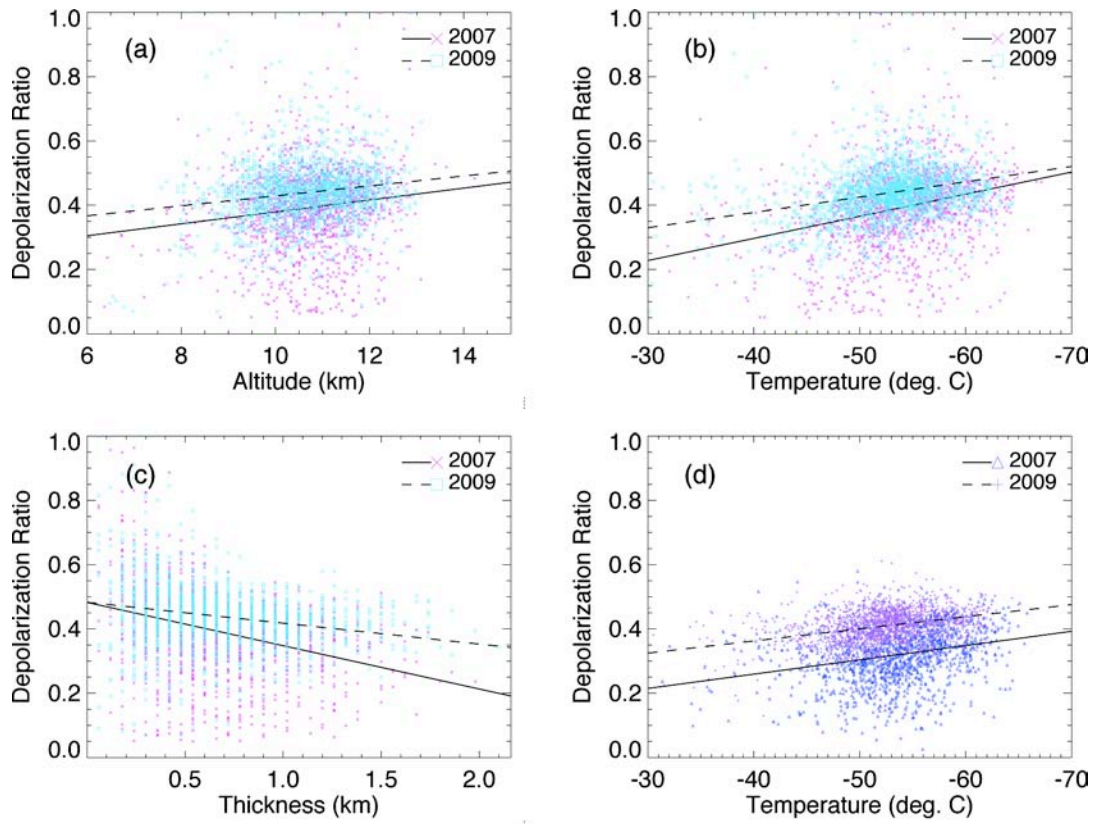


Fig. 9. Scatter plots of (a) the depolarization ratio and altitude, (b) temperature, and (c) geometrical thickness for contrails, and (d) the depolarization ratio and temperature for neighboring cirrus clouds. Least-square lines are superimposed.

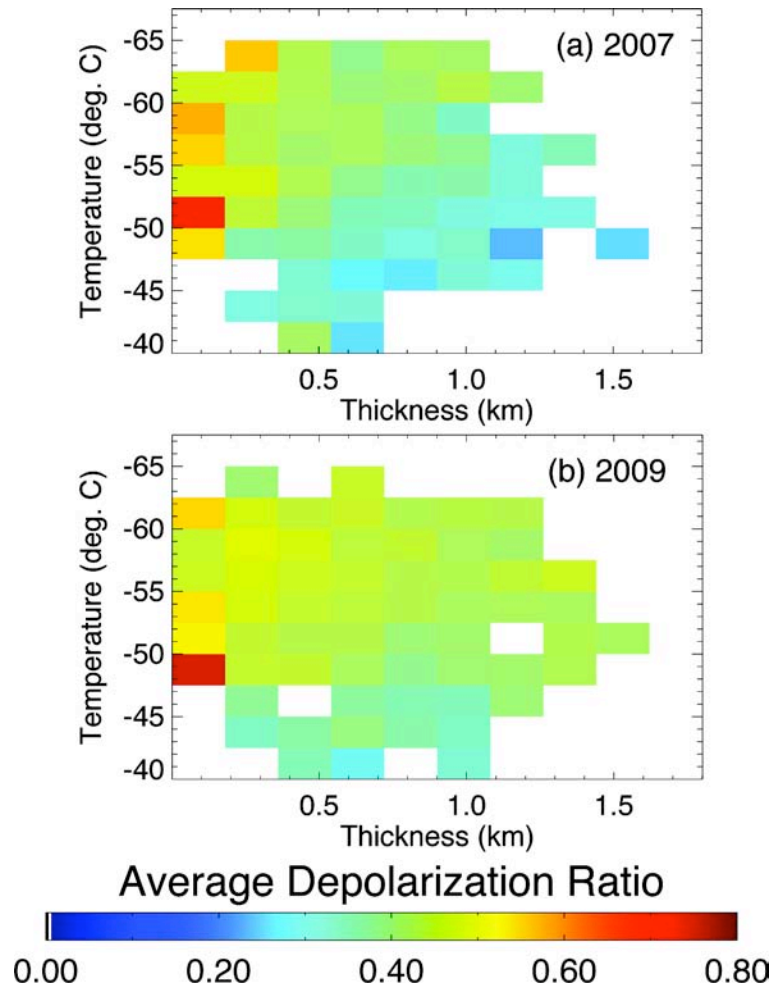


Fig. 10. Average depolarization ratio as a function of temperature and geometrical thickness obtained from measurements in (a) 2007 and (b) 2009.

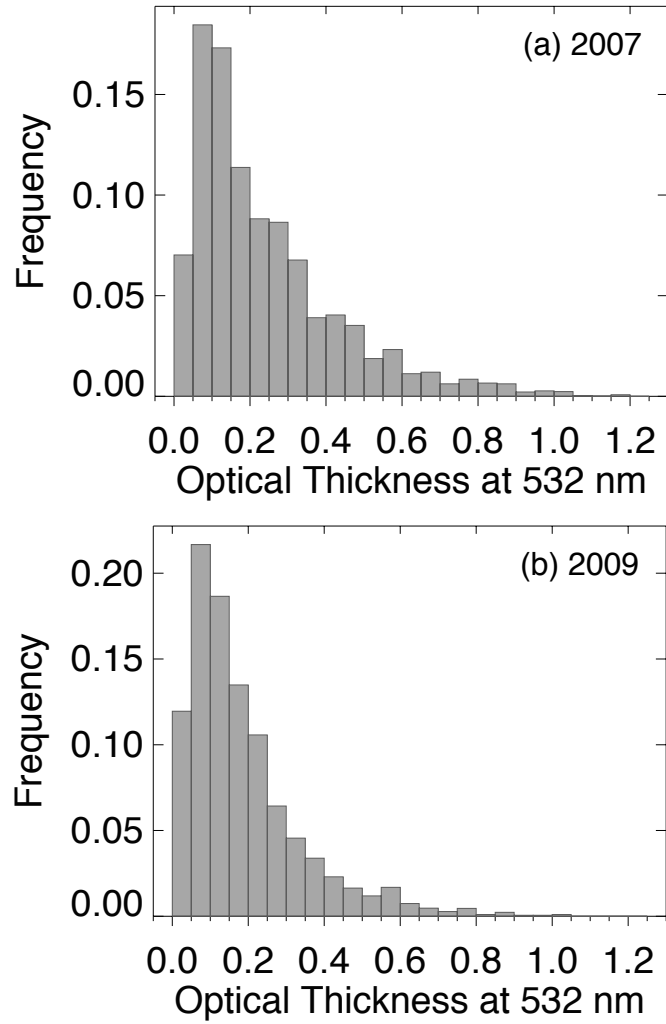


Fig. 11. Histograms of contrail optical thickness at a wavelength of 532 nm obtained from measurements in (a) 2007 and (b) 2009.

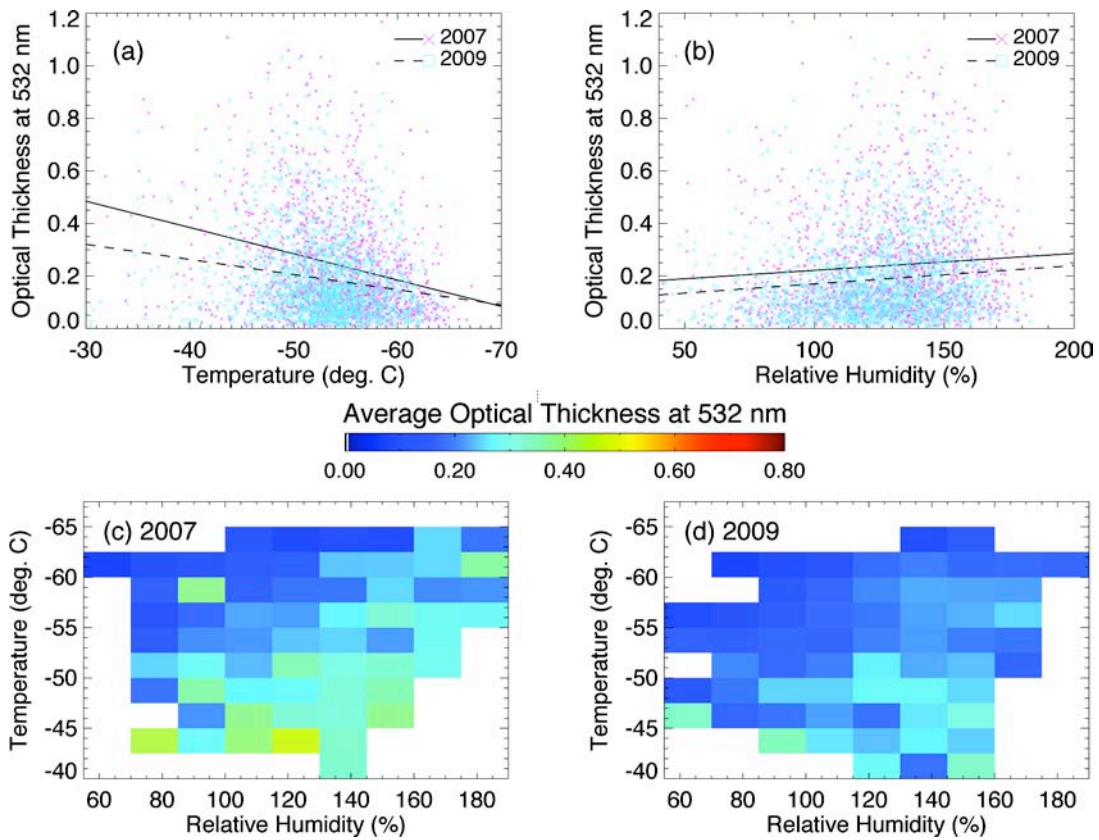


Fig. 12. The optical thickness dependence on temperature and relative humidity with respect to ice. (a) Scatter plot of optical thickness at 532 nm and temperature. (b) Scatter plot of optical thickness and relative humidity with respect to ice. (c, d) Average optical thickness at 532 nm as a function of temperature and relative humidity with respect to ice for years (a) 2007 and (b) 2009. Least-square lines are superimposed in (a) and (b).

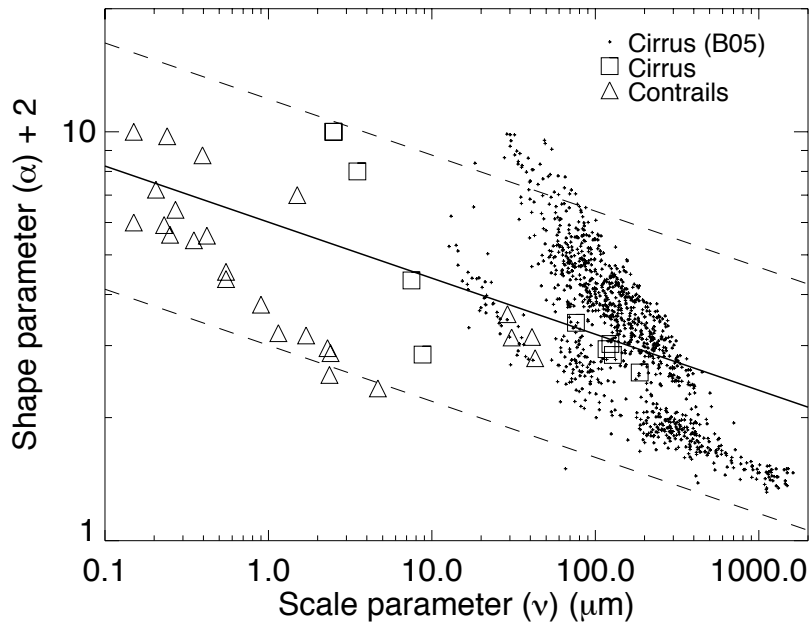


Fig. 13. Relationship between the shape parameter (α) and the scale parameter (ν) of the PSD represented by the Gamma distribution. Data obtained from in-situ measurements presented in *Baum et al.* [2005] (denoted by B05) are shown by dots. Data computed from previous in-situ measurements presented in the literature are shown by squares for cirrus clouds and triangles for contrails. The solid line denotes a least-square fit and the dashed lines denote equations with twofold $\alpha + 2$ smaller or larger values than the least-square fit.

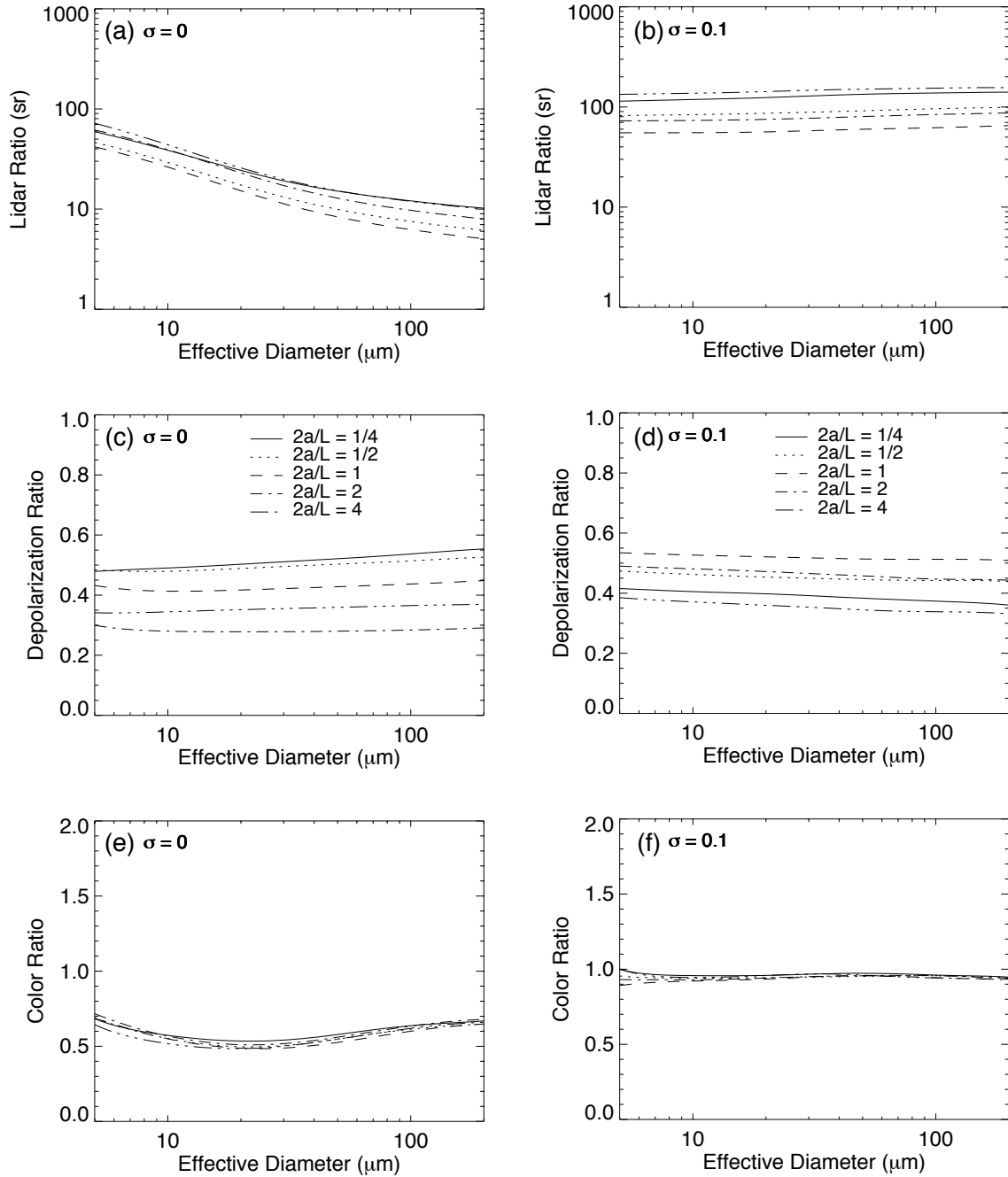


Fig. 14. Derived from IGOM calculations, (a,b) the theoretical lidar ratio, (c,d) depolarization ratio at a wavelength of 532 nm, and (e,f) color ratio as functions of the effective particle diameter for hexagonal particle polydispersions with various aspect ratios ($2a/L$). Random particle orientation is assumed. Results are shown for smooth particles ($\sigma = 0$) (a,c,e) and particles with moderate surface roughness ($\sigma = 0.1$) (b,d,f).

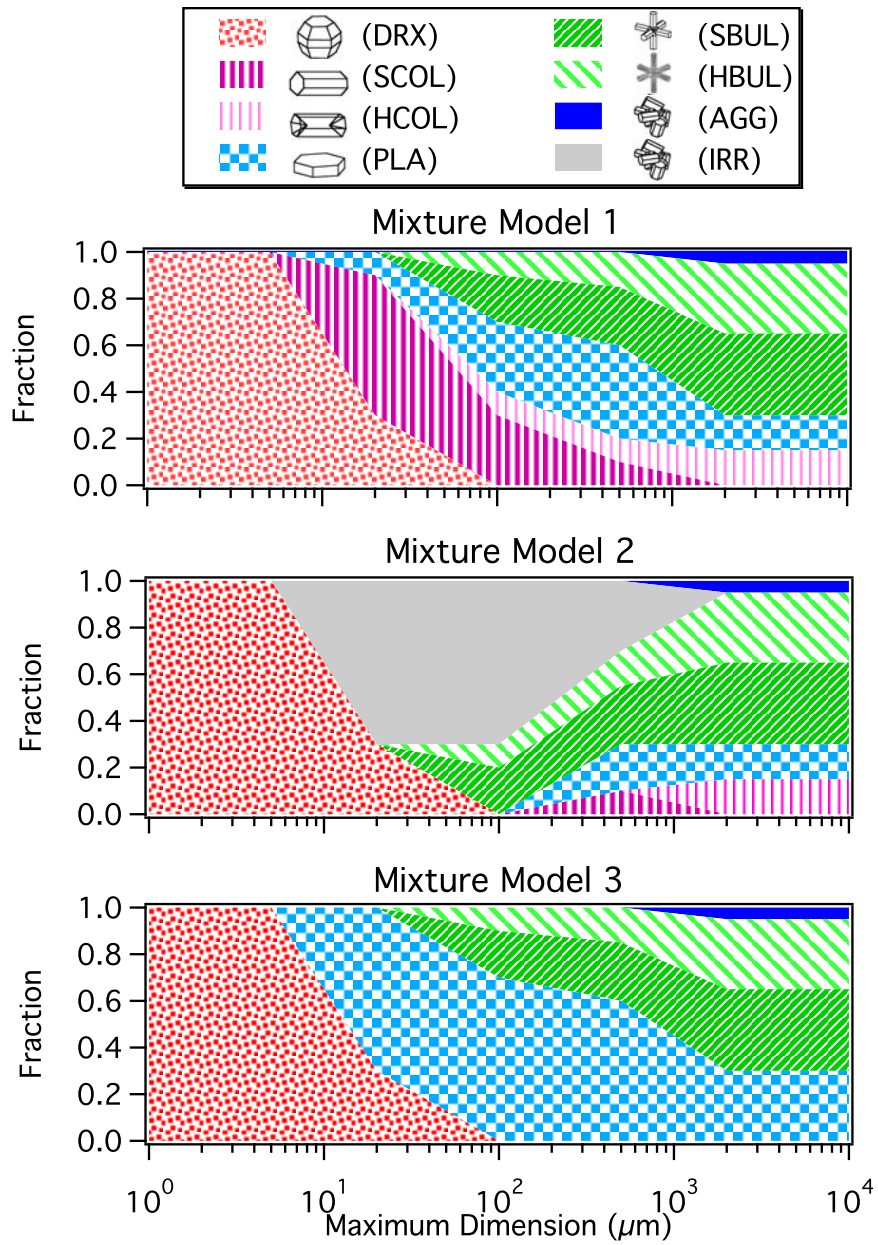


Fig. 15. Ice crystal habit fractions, as functions of the maximum dimension, for habit mixture models 1–3. Considered ice crystal habits include droxtals (DRX), solid/hollow columns (SCOL/HCOL), plates (PLA), solid/hollow bullet rosettes (SBUL/HBUL), aggregates (AGG), and irregulars (IRR).

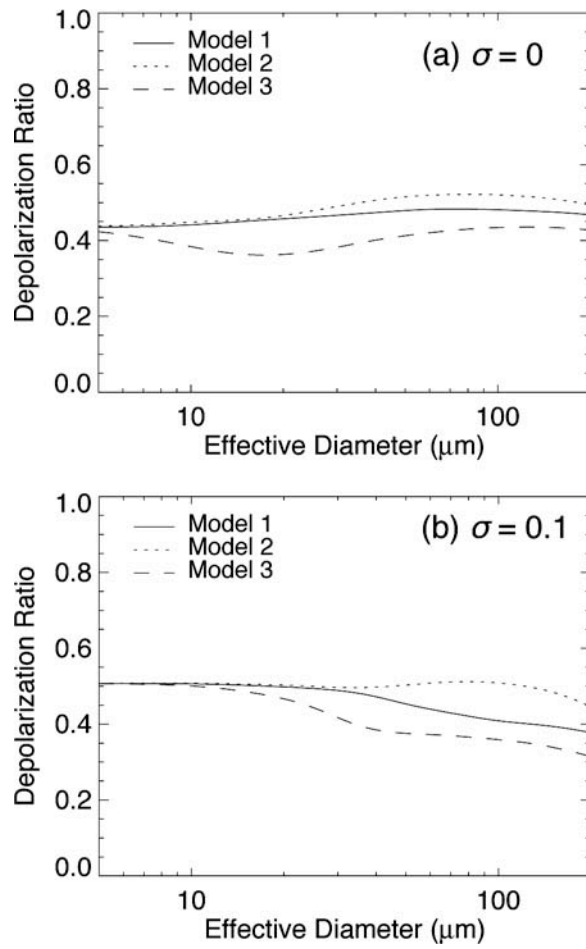


Fig. 16. Theoretical depolarization ratios at a wavelength of 532 nm as functions of effective diameter for habit mixture models (a) with and (b) without surface roughness.

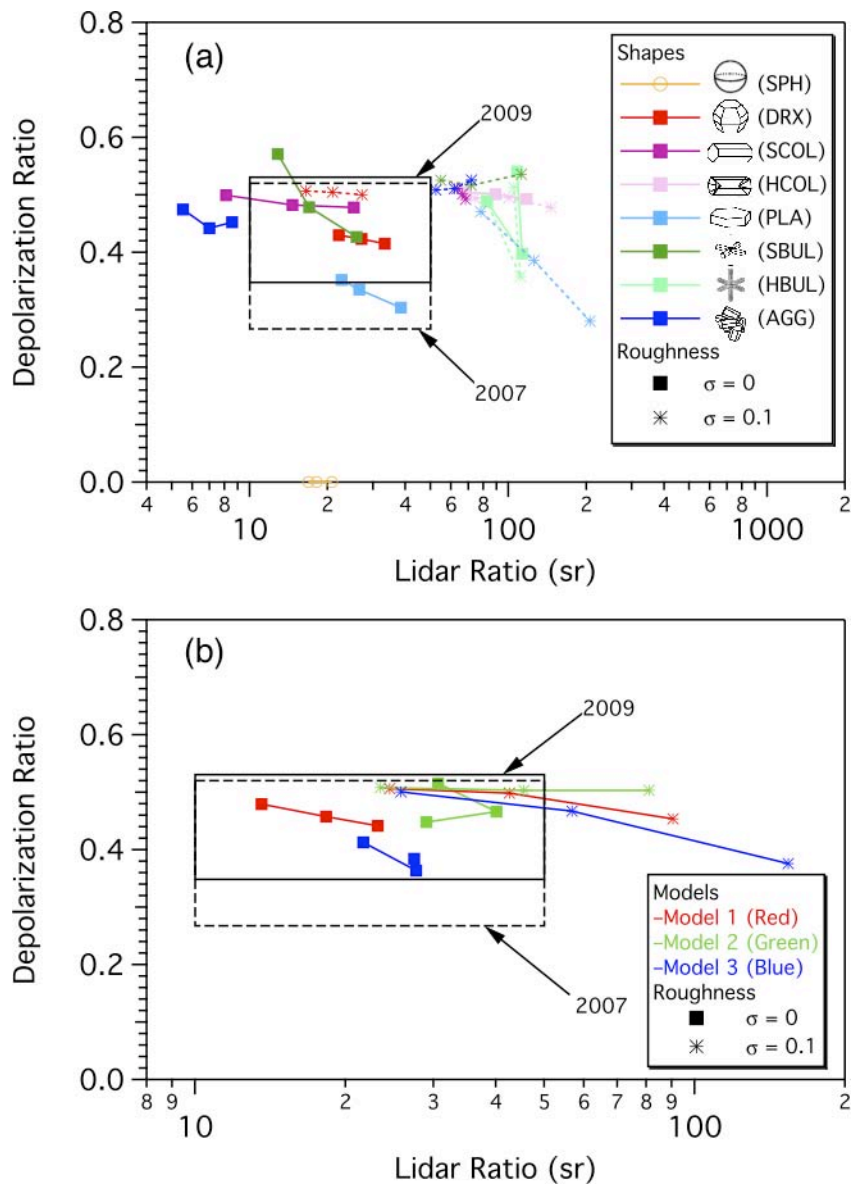


Fig. 17. Theoretical relationships between depolarization ratio and lidar ratio for (a) ice particle habits and (b) for habit mixture models. For each habit or habit mixture model, three points correspond to effective diameters of 10, 20, and 50 μm . A sphere habit is denoted by SPH, and other habit notations are the same as in Fig. 15. Superimposed rectangles denote ranges of depolarization ratio for contrails obtained from CALIOP data analysis in this study (average plus/minus one standard deviation) and a possible range of lidar ratio obtained in previous lidar measurements for contrail and optically thin natural cirrus cloud.